Article:
Henderson, S. S., Osawa, R. T., Newton, S. L. et al. (2024) An overview of the STEP divertor design and the simple models driving the plasma exhaust scenario. Nuclear Fusion. 016033. ISSN: 1741-4326

https://doi.org/10.1088/1741-4326/ad93e7

PAPER • OPEN ACCESS

An overview of the STEP divertor design and the simple models driving the plasma exhaust scenario

To cite this article: S.S. Henderson *et al* 2025 *Nucl. Fusion* **65** 016033

OPEN ACCESS
IOP Publishing | International Atomic Energy Agency
Nuclear Fusion
Nucl. Fusion **65** (2025) 016033 (18pp)
https://doi.org/10.1088/1741-4326/ad93e7

An overview of the STEP divertor design and the simple models driving the plasma exhaust scenario

S.S. Henderson[1,*], R.T. Osawa[1], S.L. Newton[1], D. Moulton[1], L. Xiang[1], R. Futtersack[1], M. Kryjak[2], C. Ridgers[2], J. Karhunen[3], A. Jarvinen[3], A. Hudoba[1], S. Bakes[1], F. Eriksson[1], H. Meyer[1], M. Lord[1], A. Tarazona[1], A. Cureton[1], A. Barth[1], B. Chuilon[1], T. Hebrard[1], S. Wang[1], Z. Vizvary[1], D. Vaccaro[1], F. Perez Smith[1], J. Farrington[1], J. Harrison[1], B. Dudson[2] and B. Lipschultz[2]

[1] United Kingdom Atomic Energy Authority, Culham Campus, Abingdon, Oxon OX14 3DB, United Kingdom of Great Britain and Northern Ireland
[2] York Plasma Institute, Department of Physics, University of York, York YO10 5DQ, United Kingdom of Great Britain and Northern Ireland
[3] VTT Technical Research Centre of Finland, Espoo FI-02044 VTT, Finland

E-mail: stuart.henderson@ukaea.uk

Received 23 July 2024, revised 7 November 2024
Accepted for publication 18 November 2024
Published 29 November 2024

Abstract

This paper presents a comprehensive overview of the preliminary divertor design and plasma exhaust scenario for the reactor-class Spherical Tokamak for Energy Production project. Due to the smaller size of the machine, with a major radius less than half that of most DEMO concepts, the current design features a double-null divertor geometry, comprising tightly baffled extended outer legs and shorter inner legs approaching an X-divertor. Leveraging a significant database of SOLPS-ITER simulations, the exhaust operational space is mapped out, offering valuable insights into the plasma exhaust dynamics. An approach involving the validation of simple, yet robust models capable of accurately predicting key exhaust parameters is detailed, thereby streamlining the design process. The simple models are used to simulate the entire plasma scenario from the plasma current ramp-up, through the burning phase, to the plasma current ramp-down. Notably, the findings suggest that pronounced detachment, with peak heat loads below engineering limits and electron temperatures below 5 eV, is achievable with a divertor neutral pressure between 10 Pa and 15 Pa during the burning phase, and pressures below 5 Pa during the ramp-up to maximise the auxiliary current-drive efficiency. Throughout the scenario, an Ar concentration of ≈3% in the scrape-off layer (SOL) is required, in combination with a core radiation fraction of 70% driven by intrinsic emission and extrinsic injection of Xe seeded fuelling pellets. However, significant uncertainties remain regarding key parameters such as the SOL heat flux width, Ar screening, and plasma kinetic effects.

* Author to whom any correspondence should be addressed.

Keywords: STEP, fusion, divertor, exhaust, reduced models

(Some figures may appear in colour only in the online journal)

1. Introduction

The design of divertors in reactor-class tokamaks is receiving significant attention, driven by progress made by ITER [1] and tokamak DEMO activities carried out in Europe, Japan, China, Korea, and the USA [2]. The challenge of maintaining first wall loads within engineering limits is more severe in DEMO compared to ITER [3, 4]. Although this might suggest a need to modify the divertor design to handle higher loads, most DEMO concepts prioritise minimising risk in extrapolation. Consequently, they adopt the conventional divertor concept following the ITER design, featuring a single-null (SN) divertor with vertical targets [1, 5, 6]. Nonetheless, alternative divertor concepts have also been explored as an option for the EU-DEMO [7–10].

The Spherical Tokamak for Energy Production (STEP) aims for a fusion gain of $\leqslant 10$, with fusion power between 1.5 GW and 1.8 GW [11, 12]. In the current design iteration, the major and minor radius are $R_0 = 3.6$ m and $a_{\min} = 2$ m, respectively. The operating scenario is expected to be H-mode, with the L-H transition occurring shortly after the non-inductive current ramp-up begins at $\approx 2-3$ MA. The plasma current will then be non-inductively ramped up to $\approx 20-25$ MA, with a toroidal field on the geometric axis $B_0 = 3.2$ T, a high elongation $\kappa \approx 3$, and a triangularity $\delta \approx 0.5$. Up to $\approx$150 MW of auxiliary current drive power, through electron cyclotron resonance heating, will be required. Combined with alpha heating, this results in $\approx$485 MW of exhaust power.

Consistent with most DEMO concepts [13], radiative cooling is planned through a combination of intrinsic radiation and the injection of Xe-doped pellets and Ar gas puffing. A core radiation fraction of 70% is expected, resulting in $\approx$150 MW of power crossing the core boundary into the scrape-off layer (SOL). This value is similar to predictions for the baseline EU-DEMO [3]. However, as a spherical tokamak (ST) with a smaller major radius, there is less physical space to distribute the power, particularly on the inboard side. For context, if STEP adopted a conventional divertor design, then the unmitigated heat flux would be approximately twice as high on the outboard divertor and three times higher on the inboard divertor compared to DEMO concepts, assuming equivalent upstream conditions.

To manage the significantly higher unmitigated heat flux expected in a SN design, the current baseline STEP design features an up-down symmetric double-null (DN) divertor. This configuration brings the unmitigated heat flux to the outer divertors in line with DEMO, while the heat flux to the inner divertors will be $\approx$50 % higher. However, controlling the vertical location of the plasma centroid within millimeters is expected to be challenging in a reactor environment, necessitating a margin for unplanned transient oscillations into a SN configuration [14]. Therefore, the design incorporates a tightly baffled extended outer divertor leg to allow for a detachment buffer without significantly impacting the core plasma. Extending the inner leg is not feasible due to engineering constraints. Consequently, the design features a moderately baffled shorter inner leg with magnetic geometry approaching an X-divertor. The engineering implications of such a design are covered separately [15, 16]. Gas valves are envisioned in both the outboard and inboard divertor regions, intended for puffing DT and D_2 to raise the divertor neutral pressure up to $\approx$15 Pa, and for introducing Ar to increase the radiation in the plasma edge, SOL, and divertor.

The primary focus of the paper is the initial scoping of the exhaust scenario and the assessment of the 2D first wall and magnetic geometry. Additionally, a database of STEP SOLPS-ITER simulations is used to validate existing 0D analytical models of the exhaust, which are beneficial for fast scoping studies of preliminary designs and scenarios [17]. A detailed discussion of 3D plasma wall effects is not yet included.

The paper is divided into two main sections: section 2 provides an overview of the operational space predicted by SOLPS-ITER simulations of three different design concepts. A set of reduced models describing key exhaust parameters is compared against the simulation database. These reduced models are then used to project the key exhaust parameters across the entire STEP scenario in section 3, including the plasma current ramp-up, the fusion burn phase during the current flat-top, and the plasma current ramp-down. Finally, known issues and uncertainties regarding the exhaust plasma scenario and further areas of design optimisation are discussed in section 4.

2. STEP exhaust operational space and reduced model validation

The STEP plasma exhaust scenario is currently being assessed using the SOLPS-ITER code [18, 19]. A substantial database of converged SOLPS simulations from multiple design iterations now exist, although a definitive SOLPS simulation for the final plasma exhaust scenario has not yet been produced. Given the lengthy convergence time of high-fidelity simulations, reduced models provide a more practical approach for evaluating all phases of the scenario and assessing the potential extreme conditions that may arise. This section aims to leverage the extensive STEP SOLPS database to validate a set of reduced models, which are then used to assess the exhaust operational space in section 3.

Section 2 is organised as follows. Section 2.1 provides an overview of the STEP SOLPS-ITER simulation database before introducing the key reduced models for fast exhaust prediction, which focus on detachment onset and target heat loads. To establish these reduced models, a parallel energy flux density model is first required, as it determines the scale of

power mitigation needed. This model, along with key parameters such as the SOL width and the power fractions to each divertor, is discussed in section 2.2. Section 2.3 examines the operational space of the inner divertor relative to the outer divertor, identifying the outer divertor as the limiting factor for detachment access. The models predicting outer divertor detachment onset and target heat loads are introduced and validated against SOLPS predictions in sections 2.4 and 2.5, respectively. Since target heat loads depend on upstream conditions, models for the upstream electron temperature and density are also presented in section 2.5. Finally, section 2.6 provides a prediction of detachment sensitivity.

Before examining the exhaust operational space, the boundary conditions are listed to provide context for the simulations, though they were often adjusted beyond these limits to explore the operational space and aid in simulation convergence. Certain limits for STEP have been defined, while others are extrapolated from DEMO and ITER.

- The maximum steady-state target heat load, occurring for durations long enough to achieve local thermal equilibrium ($>$15 s), is set at 10 MW m^{-2}. The peak transient heat load must not exceed 20 MW m^{-2}. These limits are consistent with ITER [1].
- Ar is planned as the primary SOL radiator, in addition to Xe-doped pellets to control the core radiation. Ne is rejected primarily due to difficulties with quick separation from hydrogenic fuel in the cyrogenic vacuum pump and N is rejected due to complexities with processing tritiated ammonia.
- A disadvantage of using Ar is that it intensifies divertor tile erosion and dust generation [20]. Maintaining a fully detached target plate temperature below 5 eV is therefore crucial to limit surface material erosion.
- The detachment state should be optimised to minimise neutral losses into the main chamber whilst providing a buffer against transient fluctuations arising from fluctuations in the power crossing the separatrix, deviations in the vertical location of the plasma centroid, or even failures in the fuelling systems.
- A limit of 400 g is set on the T_2 inventory within the cryopumps. For reference, ITER have an equivalent arbitrary administrative limit of 120 g [21]. The current working assumption for the cryopump regeneration time is 30 min, corresponding to a maximum injected flow rate of $\approx 9 \times 10^{22}$ DT s^{-1}, or $\approx 4.5 \times 10^{22}$ of T s^{-1}, disregarding the small burnt fraction of DT in the plasma core.
- The pump structure in the STEP SOLPS simulations does not extend to the cryopump inlet. Consequently, the temperature of the pumping surface is set to 580 K, matching values used in ITER SOLPS simulations [22]. This implies a maximum pump throughput of 357 Pam^3 s^{-1}, consistent with the maximum DT injected flow rate and similar to values expected for DEMO [23].
- The Ar fraction, $f_{Ar} = n_{Ar}/n_e$, in the core plasma should remain below $<<1\%$ to avoid excessive fuel dilution ($P_{fus} \propto (1 - 18 f_{Ar})^2$). Current machines typically observe an Ar enrichment of ≈ 2 [24] implying a maximum separatrix Ar fraction of $\approx 2\%$. Peripheral temperature gradient screening may increase enrichment factors beyond values observed in current machines if the neoclassical transport is dominated by Pfirsch-Schlüter transport and the temperature gradient is more than twice the density gradient [25, 26]. An upper limit of 3 % is therefore currently assumed, however further analysis is required to predict the strength of the temperature gradient screening.
- During plasma current ramp-up, minimising the upstream separatrix electron density to $15\% - 25\%$ of the Greenwald fraction enables efficient current drive. Conversely, during the current flat-top, maximizing the upstream separatrix density facilitates a high bootstrap current. Ultimately, it is not clear how the separatrix density will influence the core performance in a pellet fuelled burning plasma.

2.1. STEP SOLPS-ITER database

The STEP SOLPS-ITER database used for this analysis consists of around 50 simulations, spanning three different machine iterations in connected DN geometry, as depicted in figure 1. The simulations are described in detail by Osawa *et al* [27]; in summary, they included kinetic neutral effects, assumed spatially constant radial transport, and did not include drift terms. The radial particle transport coefficients, $D_\perp$, and the radial heat transport coefficients for the ions and the electrons, $\chi_\perp$, range between $D_\perp = 0.15 - 0.3$ m^2 s^{-1} and $\chi_\perp = 0.5 - 1$ m^2 s^{-1} in the simulations. The inclusion of spatially varying (i.e. ballooning) radial transport coefficients and particle drifts is expected to induce alterations in the power distribution between the inner and outer divertors, as well as asymmetries between the upper and lower divertors [27, 28].

To achieve fully detached conditions, Ar gas was seeded into the divertor regions and D was injected both through a core ion flux and via up–down symmetric gas puffs into the private flux regions near the X-points. The database also includes a smaller number of simulations with variations in both the Ar and D_2 gas puffing locations and with He originating from the core with a value consistent with the fusion power. All ion states of D, He, and Ar were tracked in the simulations. Only the outer divertors are actively pumped and neutrals can move freely between the inner and outer divertors through the space in the private flux region between the wall and the plasma grid. In the third design iteration, a dome structure was included with two semi-transparent dome supports (50%) to direct the neutral flow between divertors through the gap underneath the dome. The simulation set consists of cases for each design iteration with varying levels of D and Ar gas injection rates, and different input powers.

An overview of key parameters from the STEP simulation database is given in table 1. Notably, a wide range of parameters is achieved by including simulations of two additional equilibria from the plasma current ramp at approximately 2 MA and 10 MA, along with the database simulating the current flat-top at around 20 MA. As the simple models described next were originally derived from ASDEX Upgrade

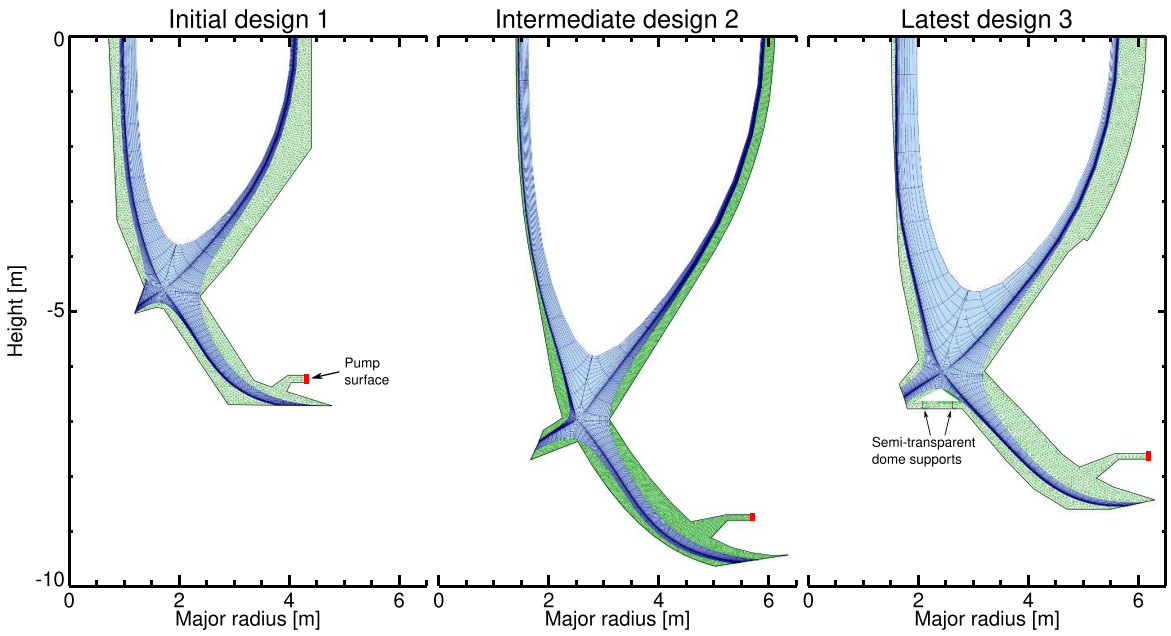

Figure 1. Baseline SOLPS-ITER simulation grids for three different STEP design iterations included in this analysis.

Table 1. Summary of key parameter ranges over which the detachment qualifier has been tested through STEP SOLPS-ITER simulations and experiments on ASDEX Upgrade [29, 30] and JET [31].

Parameter	STEP	AUG	JET
I_P (MA)	2–20	1	2.5
P_{sep} (MW)	25–200	5–12	10–15
$\lambda_{q,u}$ (mm)	1.8–12.7	$\approx 2-2.5$	$\approx 1.5-2$
L_X (m)	10–350	10	17
R_0 (m)	2.5–0.6	1.65	3.0
a_{min} (m)	1.5–2.2	0.5	1.25
p_0 (Pa)	0.6–21	0.7–2.5	1–2
c_{Ar} (%)	0–6	0–0.5	0–2
B_0 (T)	2.3–3.2	2.5	2.5

(AUG) experiments and further testing on JET, those machine parameters are also included.

2.2. Parallel energy flux density

The peak unmitigated parallel energy flux density, $q_{||}^{unmit}$, defines the scale of the exhaust challenge – specifically, the volumetric power and pressure loss required to avoid unacceptable damage or erosion of the divertor components – and is also a key parameter for determining the upstream separatrix temperature and density, as demonstrated later in equation (15) and (22). The upstream value of $q_{||}^{unmit}$, denoted by the subscript u, can be calculated using equation 5.5 from [32]:

$$q_{||,u}^{unmit} = \frac{P_{up}}{2\pi\,\lambda_{q,u}R_u}\frac{B_{Tot,u}}{B_{\theta,u}}. \quad (1)$$

$P_{up} = P_{sep}f_{div}$ where f_{div} is the fraction of power directed to the divertor (typically assumed to be $f_{div} = 1/2$ in conventional SN machines), R_u is the midplane separatrix radius, and $\lambda_{q,u}$ is the upstream near SOL parallel heat flux width. $B_{\theta,u}$ is the upstream poloidal magnetic field, which can be estimated for highly elongated plasmas (i.e. $\kappa = 3$) using $B_{\theta,u} \approx 0.31 I_P/\kappa a_{min}$, and $B_{Tot,u}$ is the upstream total magnetic field.

The equivalent value at the target, denoted by the subscript t, is calculated using the same formulation as equation (1) but replacing the upstream parameters with their equivalent target values. The total magnetic field at the target can be approximated using $B_{Tot,t} = \sqrt{B_{T,t}^2 + B_{\theta,t}^2} \approx B_0R_0/R_t$, where B_T is the toroidal magnetic field. The error from this approximation in the divertor is < 20 %, since $B_{\theta,t}$ is relatively low compared to $B_{T,t}$. Finally, relating $\lambda_{q,t}$ and $\lambda_{q,u}$ through flux expansion,

$$\lambda_{q,t} = \frac{R_u B_{\theta,u}}{R_t B_{\theta,t}}\lambda_{q,u}, \quad (2)$$

the parallel energy flux density at the target can be written as:

$$q_{||,t}^{unmit} = \frac{P_{up}}{2\pi\,\lambda_{q,t}R_t}\frac{B_{Tot,t}}{B_{\theta,t}} = \frac{P_{up}}{2\pi\,\lambda_{q,u}R_u}\frac{B_{Tot,t}}{B_{\theta,u}} \approx \frac{P_{sep}f_{div}}{2\pi\,\lambda_{q,u}R_u}\frac{R_0B_0}{R_tB_{\theta,u}}. \quad (3)$$

The unmitigated perpendicular heat load at the divertor target is then calculated as $q_{\perp,t}^{unmit} = q_{||,t}^{unmit}\sin\alpha_t$, where α_t is the grazing angle between magnetic field lines and the target surface. This equation implies that $q_{\perp,t}^{unmit}$ can be calculated with engineering parameters, except for $\lambda_{q,u}$ and f_{div} which are discussed next.

2.2.1. Near SOL power width. The near SOL power width, $\lambda_{q,u}$, is not directly predicted by SOLPS, but instead influenced by the setting of perpendicular particle and heat transport coefficients, $D_\perp$ and $\chi_\perp$, respectively. A multi-machine experimental study of H-mode scenarios consistently demonstrated

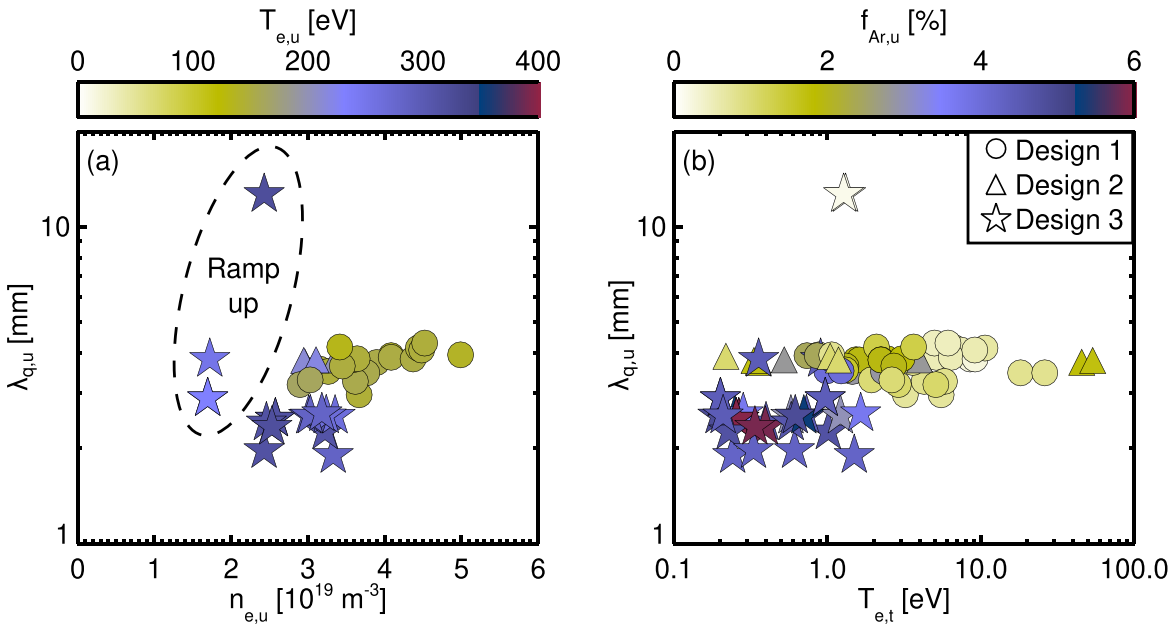

Figure 2. SOLPS simulation data outputs of the near SOL power width as a function of (*a*) the upstream separatrix electron density, with shading of the upstream separatrix electron temperature, and (*b*) the outer target electron temperature, with individual points shown for the upper and lower divertors and shading of the upstream separatrix Ar fraction $f_{\mathrm{Ar,u}} = n_{\mathrm{Ar,u}}/n_{\mathrm{e,u}}$.

that $\lambda_{\mathrm{q,u}}$ is inversely proportional to $B_{\theta,\mathrm{u}}$ [33], leading to the conclusion that future reactors operating at high I_{P} (and thus high $B_{\theta,\mathrm{u}}$) would likely operate with extremely narrow SOL widths < 1 mm. Predictions of the SOL heat flux width over the entire STEP scenario (i.e. ramp-up, flat-top, ramp-down) are assessed in section 3 using empirical scalings [33–35] and the Heuristic Drift (HD) model [36]. For the flat-top phase, empirical models predict the narrowest values, around 0.5 mm, while the HD model estimates a range of 2–4 mm.

The analysis provided in appendix suggests that the most likely values for $\lambda_{\mathrm{q,u}}$ on STEP range from 1–2 mm, though values as low as 0.5 mm or as high as 4 mm are not ruled out. Achieving such narrow SOL widths in SOLPS, however, requires very low perpendicular transport values, which increases simulation convergence time. As a result, the initial simulations for the first design iteration started with moderately high radial transport ($D_\perp = 0.3\,\mathrm{m^2\,s^{-1}}$ and $\chi_\perp = 1\,\mathrm{m^2\,s^{-1}}$), corresponding to $\lambda_{\mathrm{q,u}} = 3-4$ mm. These values have been gradually reduced to $D_\perp = 0.15\,\mathrm{m^2\,s^{-1}}$ and $\chi_\perp = 0.3\,\mathrm{m^2\,s^{-1}}$, leading to $\lambda_{\mathrm{q,u}} = 1.8-2$ mm in the most recent design. A summary of the SOLPS operational space in terms of $\lambda_{\mathrm{q,u}}$, along with the associated upstream separatrix densities and temperatures, is shown in figure 2(*a*), while the upstream Ar fractions and peak divertor temperatures are shown in figure 2(*b*). Ongoing simulations aim to further reduce $\lambda_{\mathrm{q,u}}$ toward values closer to 1 mm; section 3 assesses the implications of narrower SOL widths using reduced models.

2.2.2. Power sharing between divertors. In conventional tokamaks, with SN geometry, the fraction of power directed to the outer divertor is typically estimated as $f_{\mathrm{div}} = 0.5$. This fraction differs significantly in STs, both in DN and SN geometry, and can also be impacted by upstream radiation. The value of f_{div} is calculated from SOLPS simulation output by integrating the unmitigated load at the divertor target over the mesh area and dividing by P_{sep}. The power fraction to the inner and outer divertors calculated from the SOLPS output is shown in figure 3(*a*). Due to radiation in the SOL above the divertor entrance, f_{div} is dependent on the Ar concentration, c_{Ar}, and the electron density, n_{e}. c_{Ar} is calculated by taking the volume average, defined over a region R of cells of volume V as:

$$c_{\mathrm{Ar}} = \frac{\sum_R V\left(\sum_Z n_{\mathrm{Ar}^Z} + n_{\mathrm{Ar}^0}\right) / \left(n_{\mathrm{D}^+} + n_{\mathrm{D}^0} + 2n_{\mathrm{D}_2^0}\right)}{\sum_R V}. \quad (4)$$

For the Ar concentration, the region is defined across three cells, specifically one cell from each of the first three flux tubes in the SOL. These cells are chosen corresponding to where the radiation is at its maximum between the target and midplane in each flux tube. Using c_{Ar} and the divertor neutral pressure at the pump duct, $p_{0,\mathrm{duct}}$, as a proxy for the upstream electron density, f_{div} is approximated by the dashed line in figure 3(*a*). The best-fit equation is

$$f_{\mathrm{div}} \approx f_{\mathrm{div,max}} - 0.8\times10^{-3}\,(1+90c_{\mathrm{Ar}})\,p_{0,\mathrm{duct}}, \quad (5)$$

where $f_{\mathrm{div,max}}$ is approximately 0.08 and 0.4 for the inner and outer divertors, respectively. As shown in the next subsections, the factor $(1+90c_{\mathrm{Ar}})p_{0,\mathrm{duct}}$ is also an effective parameter to gauge the detachment access across the simulation database.

A comparison of $q_{||,\mathrm{t}}^{\mathrm{unmit}}$ calculated using equation (3) and inferred directly from SOLPS-ITER output $q_{||,\mathrm{t}}^{\mathrm{unmit}}$ for both the inner and outer targets is shown in figure 3(*b*). For this comparison, $\lambda_{\mathrm{q,u}}$ is determined from the SOLPS output using

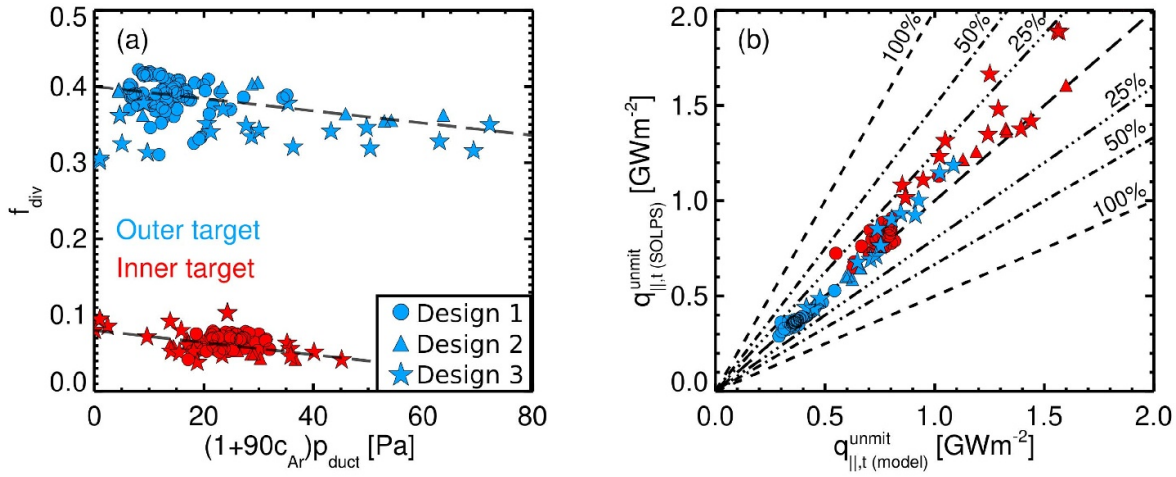

Figure 3. (*a*) Unmitigated power fraction directed to each divertor as a function of the divertor duct neutral pressure multiplied by the Ar concentration and radiation efficiency and (*b*) a comparison of the SOLPS-ITER and calculated (see equation (3)) unmitigated target heat load. Best fit dashed lines in (*a*) are described in the text.

$\lambda_{q,u} = \frac{1}{q^{unmit}_{||,t}} \int q_{||,t} dr$, where the integral is over the perpendicular radial coordinate at the midplane from the separatrix to the far SOL. While perfect agreement between the two quantities might be expected, given that simulation outputs of $\lambda_{q,u}$ and f_{div} are used in equation (3), this is not guaranteed. Since $\lambda_{q,u}$ is not a direct simulation output and requires post-processing, and due to simplifications in the calculation of $B_{T,u}$, it is important to verify that the modelled values reproduce the simulation outputs within the expected uncertainy range of < 20 %. The scatter in inner target predictions is likely due to the smaller inboard target impacting the integral for the calculation of $\lambda_{q,u}$. Notably, the values shown in figure 3(*b*) indicate that, even with DN geometry, the inner divertor values of $q^{unmit}_{||,t}$ are ≈ 2x greater than those of the outer divertor.

2.3. Inner divertor operational space

In conventional tokamaks, it is typically assumed that the outer divertor detachment is the limiting factor, with the inner divertor detaching significantly earlier. Given the significantly high values of $q^{unmit}_{||,t}$ at the inner divertor, this subsection evaluates the validity of this assumption in cases with different inner divertor configurations.

In the initial STEP design, two additional inner divertor configurations were considered alongside the standard inner vertical target (IVT): an inner horizontal target (IHT), and an inner X-divertor (IXD). A fixed outer horizontal target (OHT) was used in all simulations. Figure 4 illustrates the inner divertor geometry and simulation mesh for the three configurations, showing total (D and D_2) density contours, as well as inner target temperature and density profiles. The simulations shown have comparable upstream electron densities $n_{e,u} \approx 3.5 \times 10^{19}$ m^{-3}, heat flux widths $\lambda_{q,u} \approx 3-4$ mm, and powers crossing the separatrix of $80-100$ MW. Both the IVT and IXD simulations included similar levels of Ar seeding to induce (partial) detachment, while the IHT was fully detached without introducing any Ar.

For the IVT shown in figure 4(*a*), the ion temperature profile along the inner divertor target indicates partial detachment, with high electron density and low ion temperatures ($\leqslant 1$ eV) in the near SOL, and low electron density with high ion temperatures (50–100 eV) in the far SOL. These high ion temperatures could lead to unacceptable erosion from Ar ions [20]. Figure 4(*a*) also shows that the IVT has the highest neutral compression, as indicated by the significant difference between the neutral and molecular density contours in the inner main chamber and divertor.

In the IHT shown in figure 4(*b*), the poloidal target angle increases recycling into the far SOL, resulting in uniformly higher neutral density across the target and fully detached conditions, which reduces the peak electron density. In contrast, neutral compression is significantly lower in the IHT, with similar density levels observed in both the inner main chamber and divertor.

Finally, the inner target conditions presented in figure 4(*c*) show that the IXD performance falls between that of the IVT and IHT. The increased flux expansion promotes more recycling into the far SOL compared to the IVT, though not as significantly as the IHT. Consequently, the far SOL remains weakly attached at ≈ 10 eV, with neutral compression similar to the IVT. For these reasons, the IXD was selected as the best compromise for the latest design. Although this assessment was based on simulations with SOL widths ranging from 3 to 4 mm, the conclusions are unlikely to change significantly at lower values.

Figures 5(*a*) and (*b*) provide an overview of the simulation results for near SOL and peak ion temperatures in the outer and inner divertors, based solely on simulations from the initial design. The results are presented as functions of $p_{0,duct}$ and

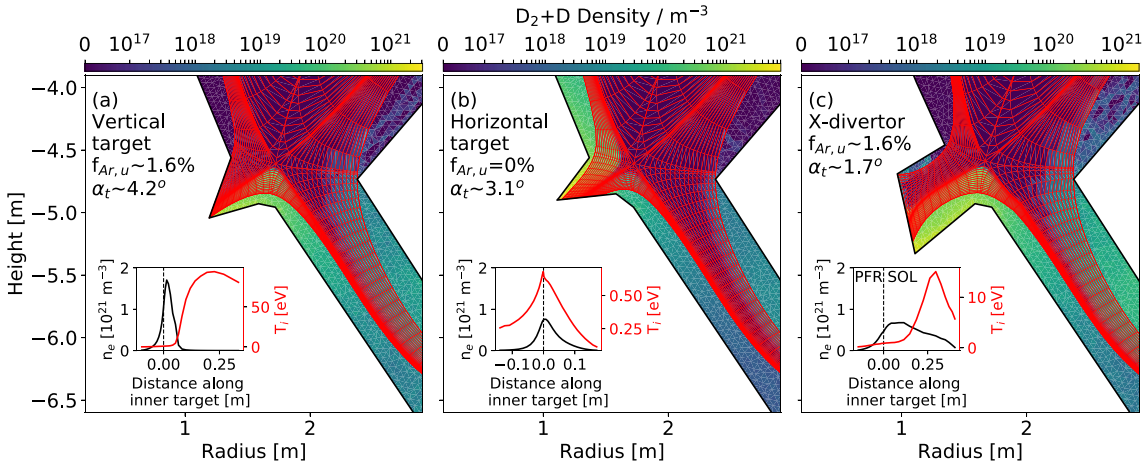

Figure 4. Overview of inner leg geometries modelled using SOLPS-ITER to assess inner leg detachment, showing three different configurations: (*a*) inner vertical target (IVT), (*b*) inner horizontal target (IHT), and (*c*) inner X-divertor (IXD). These simulations had 100 MW of input power applied, $\lambda_{q,u} \approx 3-4$ mm, and $n_{e,u} \approx 3.5 \times 10^{19}$ m^{-3}. Ar seeding was applied in both the IVT and IXD scenarios, while the IHT was D puffing only. The contours represent total neutral and molecular densities, while the insets display profiles of the electron density and ion temperature along the inner target. The inner target grazing angle is shown for each configuration.

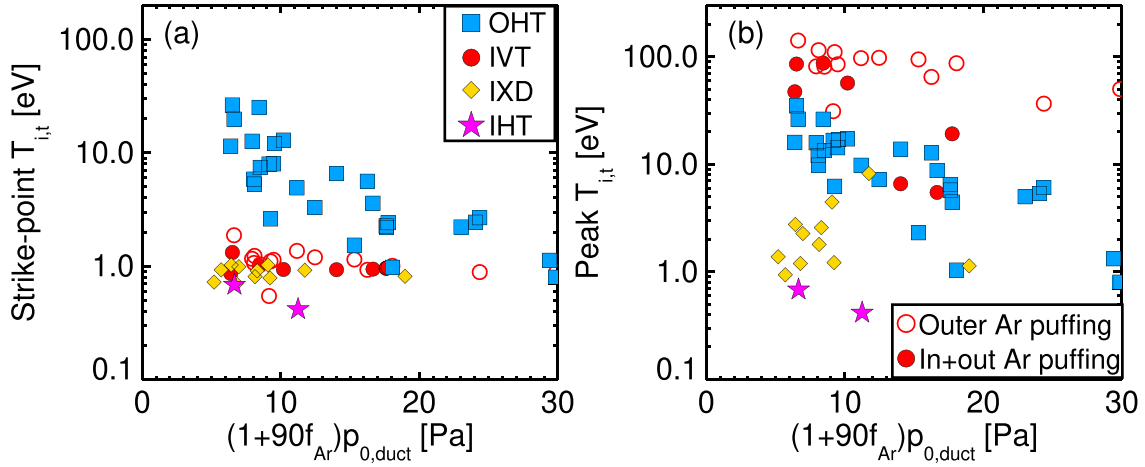

Figure 5. SOLPS outputs of the ion temperature in the inner and outer divertors. The near SOL peak value is shown in (*a*) while the peak value across the entire target is shown in (*b*).

$f_{\mathrm{Ar,u}}$, serving as a proxy for detachment access. Figure 5(*a*) shows that the near SOL inner target temperature is consistently $\approx\leqslant 1$ eV across all three inner divertor configurations, while the outer target temperature only reaches ≈ 1 eV at the highest values of $f_{\mathrm{Ar,u}}$ and $p_{0,\mathrm{duct}}$. Figure 5(*b*) demonstrates that the peak divertor temperature of the IHT and IXD is consistently lower than that of the outer target, whereas the IVT exhibits a consistently higher peak temperature. Notably, the position of the Ar seeding gas valve significantly impacts the peak ion temperature, as evidenced by the differences between the filled and unfilled symbols in figure 5(*b*). Whilst comparable cases from the initial design were used above, the trends discussed held across the simulation database for each configuration.

In summary, this analysis demonstrates that the outer target can be considered the limiting factor when evaluating reduced models for detachment.

2.4. Outer divertor detachment qualifier

To quickly predict the outer divertor detachment onset, a simple equation developed by Kallenbach *et al* [37] is compared to the STEP SOLPS simulation outputs. The equation is derived from a 1D model representing a flux bundle of the outer SOL with an upstream width of $\lambda_{q,u}$ and a downstream width in the divertor of $\lambda_{\mathrm{int}} \approx \lambda_{q,u} + 1.64S$, where S represents a broadening factor of the power decay width (e.g. by turbulence). The equation can be written in the form of a detachment qualifier, q_{det}, representing pronounced detachment for $q_{\mathrm{det}} < 1$:

$$q_{\mathrm{det}} = 1.3\frac{P_{\mathrm{sep}}}{R_0}\left(\frac{5\,\mathrm{mm}}{\lambda_{\mathrm{int}}}\right)\left(\frac{1.65\,\mathrm{m}}{R_{\mathrm{maj}}}\right)^{r_z} \times \left(\left(1+\sum_z f_z c_z\right)p_0\right)^{-1} \times \left[\frac{1}{\mathrm{Pa,\,m,\,MW}}\right]. \quad (6)$$

p_0 is the sub-divertor neutral pressure, which scales with the fuelling rate divided by the pumping speed in steady state. The normalising units within each bracketed term are chosen based on the experimental values in which the model was originally validated. It was shown on AUG that the measured sub-divertor pressure was approximately equal to the neutral pressure measured at the outer divertor target in fully detached L-mode plasmas [38]. c_Z is the impurity concentration in the SOL, and f_Z is the impurity radiation efficiency, characterising its ability to radiatively induce detachment compared to D ($f_N = 18$, $f_{Ne} = 45$, $f_{Ar} = 90$). The exponent, r_z, accounts for weak scaling with connection length. In this analysis, $r_z = 0.043$ is chosen, consistent with the value reported by Kallenbach *et al* (see table 1 [37]), which was derived assuming a fixed divertor length $L_{div} = 5$ m, without scaling for machine size. Note, the connection length scaling exponent for the detachment threshold when discussed in terms of separatrix density is observed to be $\approx 4/7$ [39, 40]. When rearranging equation (6) for the separatrix density, using the equation linking the divertor neutral pressure to the upstream separatrix density (see equation (21) and corresponding discussion in section 2.5.2), the scaling with connection length gives an exponent of ≈0.31. Further work is needed to understand these minor differences in connection length scaling.

Radiation efficiencies were determined by using a non-coronal enhancement to the impurity radiation, approximated by setting the non-coronal parameter $n_e\tau = 0.5 \times 10^{20}$ m^{-3}ms for each impurity [41]. This value was determined from results in N seeded experiments on AUG [29]. In reality, impurity transport may be different for each impurity resulting in differences to the radiation efficiencies. Recent experimental results on AUG provide evidence that $f_{Ar} > 90$ [30], but on JET the experimental evidence was consistent with $f_{Ar} = 90$ [31]. For this analysis, it is assumed that $f_{Ar} = 90$.

An outer/inner power sharing ratio of 2:1 is implicitly assumed in equation (6), which is not valid for DN geometries or SN STs [27, 42, 43]. Equation (6) is therefore divided by the power fraction directed to the outer divertor on AUG, $f_{div} = f_{SOL} f_{wall} = 0.42$, which is derived from assuming two thirds of the power directed to the outer divertor $f_{SOL} = 0.66$ and a fraction $f_{wall} = 1 - 1/e$ lost to the wall [37, 44].

The temperature at the baratron location in AUG is assumed to be 300 K, while the pumping surface in the STEP SOLPS simulation is set to 580 K. This difference in temperature will scale the pressure by a factor 1.93 relative to the AUG result. Furthermore, the divertor geometry can impact the factor difference between the average pressure near the divertor target and at the pumping duct surface, denoted Δp_{t-d}. On AUG, it is assumed that $\Delta p_{t-d} \approx 1$ in detached conditions.

Finally, R_0 is replaced by R_t and $1.65/R_0$ is replaced by the connection length between the X-point and divertor target L_X normalised by the AUG value of 12 m corresponding to the flux surface approximately 1 mm away from the separatrix at the midplane. The former accounts for total flux expansion while the latter captures changes in connection length due to plasma equilibrium and divertor design. Lastly, because the turbulence physics believed to drive the broadening of the SOL width in the divertor is not included in SOLPS, λ_{int} is replaced by $\lambda_{q,u}$ and normalised to the typical value of 2 mm measured on AUG at $I_P = 1$ MA [33]. Further investigation of current experiments and high-fidelity turbulence modelling is required to predict the broadening in a tightly baffled, extended divertor leg. With these adjustments, equation (6) becomes:

$$q_{det} = 3 \times \frac{P_{sep} f_{div}}{R_t} \left(\frac{2\,\text{mm}}{\lambda_{q,u}}\right) \left(\frac{12\,\text{m}}{L_X}\right)^{0.043} \times \left(\left(1 + \sum_Z f_Z c_Z\right) \Delta p_{t-d} p_0 \left(\frac{300\,\text{K}}{T_{pump}}\right)\right)^{-1}. \quad (7)$$

To assess this simple model for detachment, the outer divertor parameters from the SOLPS simulation need to be extracted in a consistent way. The neutral pressure is defined at the pump duct in the simulation, as shown in figure 1, following the original experiment definition. Assuming particle balance, where the injected gas puffing and pellet flow rate (the latter represented by a core ion flow across the separatrix in the SOLPS simulations) equals the pumped flow, and a molecular flow at the pump duct, the neutral pressure at the pump duct can be calculated using:

$$p_0 = \frac{\Phi_{puff} + \Phi_{pellet}}{2S} k_B T_{pump}. \quad (8)$$

S is the total pump speed and Φ denotes the flow rate in particles per second, both of which are set as inputs in the SOLPS simulations. The temperature at the pump duct location, T_{pump}, is set to 580 K in the SOLPS-ITER simulations, matching values used in ITER simulations [22]. The pressure at the pump duct from the simulation is calculated by averaging the total pressure, scaled to 580 K, in Eirene grid cells located within the narrow duct volume. Similarly, Δp_{t-d} is calculated by averaging the total scaled pressure in the Eirene grid cells spanning the divertor volume underneath the pump duct opening where the gas temperature is ≈ 1160 K (i.e. matching the non-pumping wall temperature). Typically, this factor is ≈2 across the different geometries studied in the database and converges to unity after the plasma detaches.

An overview of the results from the database is shown in figure 6. The comparison is kept only to the outer divertor since there is no obvious location on the grid to define the neutral pressure for the inner divertor as it is not pumped. The inner divertor was discussed separately in section 2.3. The detachment qualifier model, $q_{det} = 1$ manages to robustly predict the detachment point of the outer divertor, defined as the point at which the peak target temperature, $T_{e,t}$, falls to approximately 1 − 2 eV, as shown in figure 6(*a*). The dashed line corresponds to an analytical fit of the points:

$$q_{det} = 10^{0.54 \log_{10}(T_{e,t}) - 0.11}. \quad (9)$$

The points shown in figure 6 only include cases with D_2 puffing from underneath the X-points, or with a mixture of D_2 puffing from underneath the X-points and from the midplane.

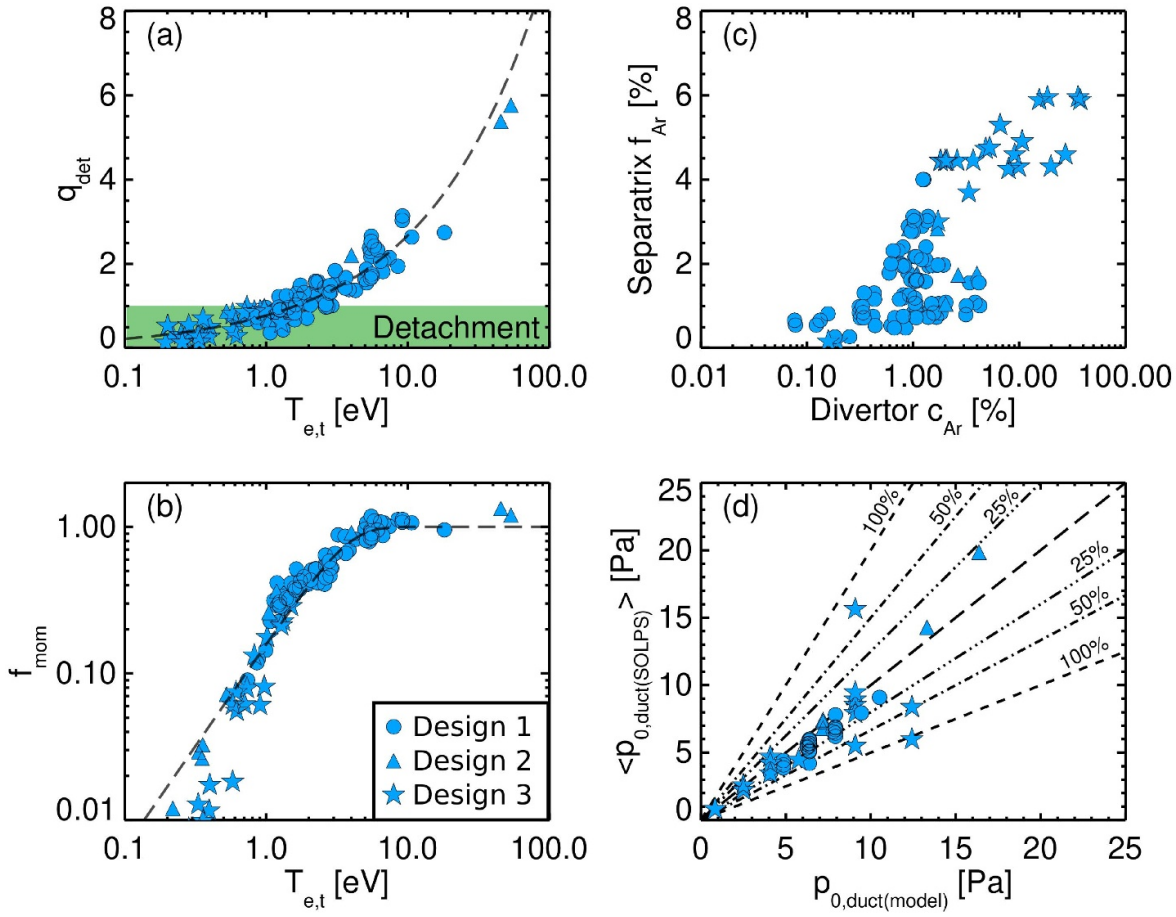

Figure 6. Comparison of the outer divertor detachment qualifier (*a*) and momentum loss (*b*) as a function of peak divertor temperature. (*c*) Provides a comparison of the midplane separatrix average Ar concentration and value used to calculate q_{det} and (*d*) compares the simulation duct pressure with simple estimates from particle conservation. Best fit dashed lines in (*a*) and (*b*) are shown to highlight the ordering of q_{det} and f_{mom} with the target temperature.

Cases with strong D_2 puffing from the midplane were investigated but are not shown in the figure. Interestingly, they demonstrated a clear deviation from the dashed line in figure 6(*a*), with target temperatures as high as 10 eV for $q_{det} < 1$. This likely indicates a change in radiation efficiency, which should be considered if midplane D_2 puffing is planned.

Detachment is expected to coincide with a drop in pressure between the midplane and divertor [45, 46]. The momentum loss factor, f_{mom}, can be expressed as:

$$f_{mom} = \frac{2T_t n_t}{T_u n_u}. \tag{10}$$

The temperatures and densities represent the sum of electron and ion contributions (i.e. $T_u = T_{e,u} + T_{i,u}$). Values of $f_{mom} < 1$ correspond to pressure loss. Figure 6(*b*) shows that f_{mom} begins to decrease below unity at $T_{e,t} = 8$ eV and reaches approximately 0.5 at $T_{e,t} \approx 2$ eV, which is in agreement with observations from experiments [46]. The dashed line in figure 6(*b*) again corresponds to a simple fit:

$$f_{mom} = \tanh\left(0.16 T_{e,t}^{1.4}\right). \tag{11}$$

Equations (9) and (11) are used to predict the target heat loads in section 3.

Next, it is important to understand how the detachment solution may impact the fusion power output, which scales as $P_{fus} \propto (1 - < Z > f_Z)^2$ where $f_Z = n_Z/n_e$. Note that the chosen c_{Ar} definition normalises the Ar density by the D density, whereas f_{Ar} normalises it by n_e. Typically, $c_{Ar} \approx f_{Ar}$ can be assumed in the divertor, however upstream c_{Ar} can vary up to unity, whereas f_{Ar} is typically limited to values below 0.06 assuming that the average Ar charge is $\approx 16 - 18$. From the simulations, f_{Ar} is volume averaged across all cells within the last closed flux ring of the core. It is expected that the f_{Ar} in the core is likely to be at least a factor two lower due to transport across the pedestal [24]. A comparison of c_{Ar} and f_{Ar} is given in figure 6(*c*). In some cases, c_{Ar} acts as a reasonable estimate of f_{Ar}; however, the scatter indicates that transport is sensitive to factors in the database, primarily concerning the gas puffing locations [47, 48].

Finally, figure 6(*d*) shows that equation (8) is a reasonable estimate of the duct pressure in the SOLPS simulation. A typical indicator of convergence in SOLPS is when the particles injected and pumped are in balance. Given that the two pump

ducts are the only defined pumping surfaces in the simulations, the level of agreement shown in figure 6(*d*) is effectively indicating the level of convergence in the simulations. A small number of simulations were included which had worse agreement in duct pressure (and hence not achieved sufficient particle balance), nonetheless these had still reached relatively steady plasma conditions.

2.5. Target heat loads

Achieving full detachment guarantees low temperatures at the target below 5 eV. A model is still required to predict the resultant peak heat loads. The target head load is calculated using the sheath boundary condition to predict the plasma kinetic load and an additional term to account for surface recombination at the target:

$$q_{\perp,\mathrm{t}} = q_{||,\mathrm{t}} \sin\alpha_\mathrm{t} = \left(\frac{2}{m_\mathrm{D}}\right)^{1/2} T_{\mathrm{e,t}} n_{\mathrm{e,t}} e^{3/2} \times \left(\gamma T_{\mathrm{e,t}}^{1/2} + \epsilon T_{\mathrm{e,t}}^{-1/2}\right) \sin\alpha_\mathrm{t}, \tag{12}$$

where γ is the sheath transmission factor, which is typically $\approx$7. Substituting the target pressure with the upstream pressure using equation (10), the target heat load can then be expressed in terms of f_mom as:

$$\begin{aligned} q_{\perp,\mathrm{t}} &= \left(\frac{\rho_{\mathrm{n,u}}\rho_{\mathrm{T,u}}}{2\rho_{\mathrm{T,t}}}\right)\left(\frac{2}{m_\mathrm{D}}\right)^{1/2} e^{3/2} T_{\mathrm{e,u}} n_{\mathrm{e,u}} f_\mathrm{mom} \times \left(\gamma T_{\mathrm{e,t}}^{1/2} + \epsilon T_{\mathrm{e,t}}^{-1/2}\right) \sin\alpha_\mathrm{t} \\ &= 5.2\times10^{-22} T_{\mathrm{e,u}} n_{\mathrm{e,u}} f_\mathrm{mom} \left(\gamma T_{\mathrm{e,t}}^{1/2} + \epsilon T_{\mathrm{e,t}}^{-1/2}\right) \sin\alpha_\mathrm{t} \times \left[eV^{-3/2}\mathrm{m^3 MW m^2}\right]. \end{aligned} \tag{13}$$

The first term in brackets is $\approx$0.33 and $\epsilon = 13.6$ eV is the ionisation potential.

The total heat load should also include contributions from radiation and neutrals. The uncertainty arising due to these missing contributions is evaluated by comparing equation (13) with the peak heat loads from SOLPS. All parameters in equation (13) are taken directly from the simulations. Firstly, agreement within 25% is found between calculations using Equation (13) and the equivalent peak loads from SOLPS, which include only plasma kinetic and recombination loads, as shown by the yellow symbols in figure 7(*a*). The total heat loads predicted by SOLPS, including contributions from neutrals and radiation, are approximately 50% higher than the equation (13) predictions when the loads fall below 5 $\mathrm{MW m^{-2}}$, as indicated by the blue symbols in figure 7(*a*). At higher peak loads, the total SOLPS heat loads tend to align with Equation (13) predictions. The underprediction at lower peak loads corresponds to detached conditions, where neutral and radiation loads become more significant.

The peak target heat loads from the STEP SOLPS-ITER database are shown as a function of peak target temperature in figure 7(*b*). Grazing angles in the database range from $4.5^\mathrm{o} - 6^\mathrm{o}$ at the outer target. Predictions of the heat load using equation (13) with $n_\mathrm{e,u} = 3.5\times10^{19}\ \mathrm{m^{-3}}$, $T_\mathrm{e,u} = 250$ eV, $\alpha_\mathrm{t} = 5.5^\mathrm{o}$, and with f_mom calculated using equation (10) are shown for comparison by the solid line, with the dashed and dashed-dot lines representing the individual plasma kinetic and recombination contributions. The steep rise in loads above 5 eV is mostly driven by the plasma kinetic load, and emphasises the need for both margin in the engineering limits and robustness in the detachment window during operation to manage fluctuations in upstream plasma conditions. Assuming the use of W monoblock technology, a grazing angle of 5.5^o would likely account for any additional global tilting of each individual cassette ($\approx 0.5^\mathrm{o}$) and toroidal bevelling on the plasma facing surface ($\approx 1^\mathrm{o}$) to protect against melting of leading edges during divertor reattachment events, unexpected ELMs, or disruptions.

STEP does not currently envision operation with ELMs. However, the risk of unexpected ELMs cannot be ruled out. To estimate their impact, the simple model to predict the ELM perpendicular energy fluence to the target given by Eich *et al* [49] can be expanded more generally, avoiding the assumption that $R_\mathrm{t} = R_0$ and assuming that the ELM energy is split evenly between the upper and lower outer divertor, as:

$$\epsilon_\perp = \Delta_\mathrm{equi} 2\pi a_\mathrm{min} \sqrt{\frac{1+\kappa^2}{2}} \times \frac{3}{2} n_\mathrm{e,ped,top} k_\mathrm{B} T_\mathrm{e,ped,top} \times \left(\frac{R_0}{R_\mathrm{t}}\right)^2 \frac{B_0}{B_{\theta,\mathrm{u}}} \sin\alpha_\mathrm{t}, \tag{14}$$

where $\Delta_\mathrm{equi} \approx 2.5$ is a geometrical factor calculated from magnetic reconstruction, and $n_\mathrm{e,ped,top}$ and $T_\mathrm{e,ped,top}$ correspond to the pedestal top density and temperature, respectively. For an electron pedestal pressure of 45 kPa, $B_0 = 3.2$ T, $B_{\theta,\mathrm{u}} = 1.4$ T, $R_0 = 3.6$ m, $R_\mathrm{t} = 5.6$ m, $a_\mathrm{min} = 2$, $\kappa = 2.8$, and $\alpha_\mathrm{t} = 5.5$o, the resultant perpendicular ELM energy fluence is $\epsilon_\perp \approx 0.4\ \mathrm{MJ m^{-2}}$. While this number could be considered under typical melting limits, generally cited as $0.5\ \mathrm{MJ m^{-2}}$ for full surface melting on perfectly aligned, unshaped tungsten divertor targets [50], it would likely be above any cracking limits. Furthermore, the model in equation (14) is typically regarded as the lower limit, with experimental results varying up to a factor 3 higher. On the other hand, recent experiments on AUG have demonstrated that impurities efficient at radiating at pedestal temperatures (i.e Ar) can radiate up to 60% of the ELM energy without degrading the core performance [51], thus potentially buffering the energy fluence directed towards the divertor. Further research is planned to understand the potential ELM energy loading, but, tentatively, scenarios with ELM suppression techniques are assumed. ELMs may be more tolerable during the ramp-up on STEP due to the lower pedestal pressure.

To predict the target heat loads using reduced model, equations are required for the upstream electron temperature and density. These equations are discussed next.

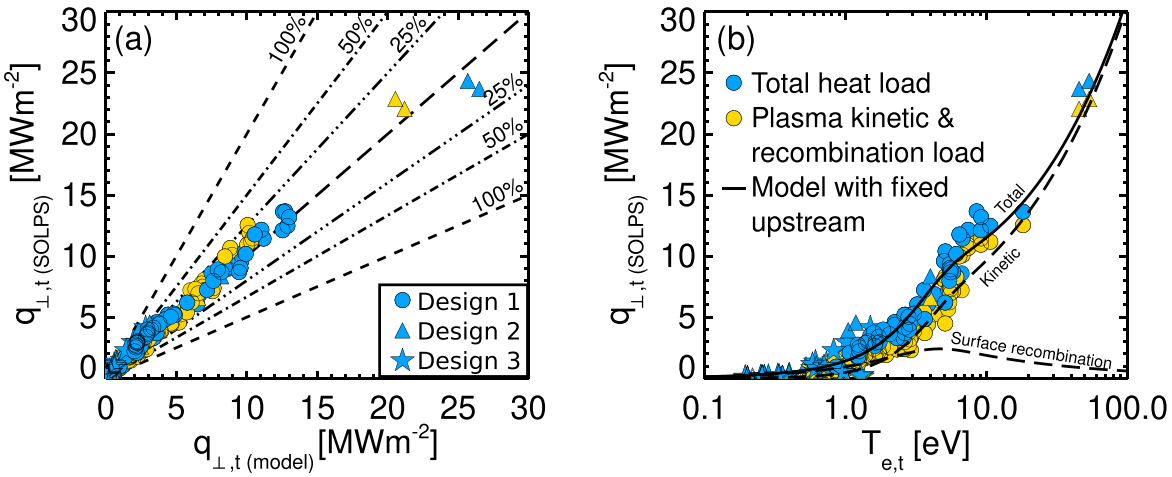

Figure 7. Peak outer target heat loads from SOLPS as a function of (*a*) calculations using equation (13) and (*b*) SOLPS peak target temperature. The yellow symbols represent the summed contribution from the plasma kinetic and recombination loads, and the blue symbols represent the total heat loads. The solid line in (*b*) represents a prediction of the heat load using equation (13) with $n_{e,u} = 3.5 \times 10^{19}\,\mathrm{m}^{-3}$, $T_{e,u} = 250\,\mathrm{eV}$, $\alpha_t = 5.5°$, and with f_{mom} calculated using equation (10). The dashed and dashed-dot lines represent the contributions from the plasma kinetic and recombination load, respectively.

2.5.1. Upstream temperature. The upstream temperature can be estimated using the 2-point (2P) model [32]:

$$T_{e,u} = \left(\frac{7 q_{||,u} L_c}{2\kappa_0 \kappa_Z}\right)^{2/7}. \tag{15}$$

L_c is the connection length between the midplane and target. κ_0 is the normalised electron parallel thermal conductivity, defined in SOLPS-ITER as $\kappa_0 = 2368\,\mathrm{Wm^{-1}eV^{-7/2}}$, and κ_Z is the finite-Z correction of the electron parallel conductivity:

$$\kappa_Z = \frac{1}{2.92} \frac{3.9 + 2.3/Z_{eff}}{Z_{eff}\left(0.31 + 1.2/Z_{eff} + 0.41/Z_{eff}^2\right)}, \tag{16}$$

where best agreement to the simulated values is found when defining Z_{eff} in the cell corresponding to the first flux tube in the SOL at the midplane. Z_{eff} can be approximated assuming a single impurity (Ar) with a dominant charge state $Z = 17$:

$$Z_{eff} = 1 + Z(Z-1)\,c_Z = 1 + 272 c_{Ar}. \tag{17}$$

Comparison of the calculated temperature and the value at the outer midplane separatrix from SOLPS is shown in figure 8(*a*). Agreement within 10% is found across a range of temperatures spanning at least a factor of two.

2.5.2. Upstream density. The 2P model is again used as a starting point to provide an expression for the midplane separatrix electron density, $n_{e,u}$. Plasma parameters in the divertor and midplane are assumed to be coupled by pressure balance and heat conduction through f_{mom} and the radiation loss factor:

$$f_{rad} = b \frac{q_{||,t}}{q_{||,u}}, \tag{18}$$

where $b = \lambda_{int}/\lambda_{q,u}$. Using $\rho_{[T,n],[u,t]}$ to relate the ratio of ion to electron quantities (i.e. $\rho_{[T,u]} = T_{i,u}/T_{e,u}$) and taking the expression for $T_{e,u}$ in equation (15) allows equation (18) to be rearranged as:

$$\begin{aligned} n_{e,u} &= \left(\frac{2\rho_{T,t}\rho_{n,t}}{\rho_{n,u}\rho_{T,u}}\right) \frac{n_{e,t} T_{e,t}}{f_{mom}} \left(\frac{2\kappa_0\kappa_Z}{7 q_{||,u} L_c}\right)^{2/7} \\ &\approx \frac{3}{2} \frac{n_{e,t} T_{e,t}}{f_{mom}} \left(\frac{2\kappa_0\kappa_Z}{7 q_{||,u} L_c}\right)^{2/7}, \end{aligned} \tag{19}$$

where the terms in the first bracket reduce to $\approx 3/2$. $n_{e,t}$ is then replaced using equation (12), with the surface recombination term being neglected for simplification.

Kallenbach *et al* [52, 53] introduce the assumption that the bulk ion and neutral particle flux densities are equal in the strike-point region, which was applicable to the 1D geometry but cannot be expected for realistic divertor geometries. The uncertainty is therefore discussed below with respect to this. Following this methodology, the neutral particle flux density, Γ_0, can be written as:

$$\Gamma_0 = \begin{cases} \frac{\sin\alpha_t q_{||,t}}{\gamma e T_{e,t}} = \frac{f_{rad}\sin\alpha_t q_{||,u}}{\gamma b e T_{e,t,}}, & \text{at outer divertor target} \\ \frac{2\Delta p_{t-d} p_0}{k_B T} \frac{<v>}{4} = \frac{2\Delta p_{t-d} p_0}{4 k_B T}\sqrt{\frac{8 k_B T}{\pi m_{D_2}}} = 1.1\times 10^{23}\Delta p_{t-d} p_0, & \text{at pump duct.} \end{cases} \tag{20}$$

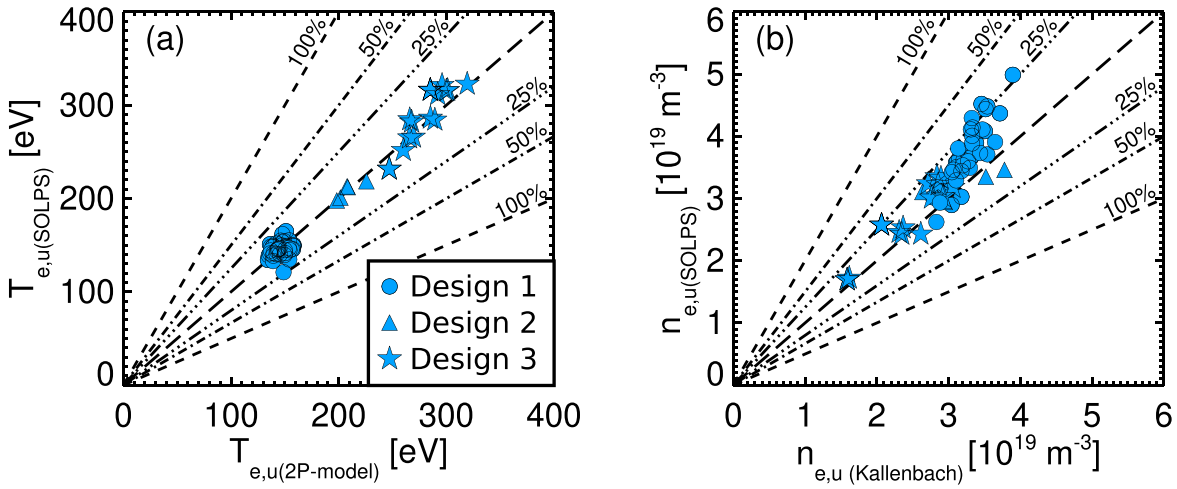

Figure 8. Comparison of simulated upstream electron temperature (*a*) and density (*b*) to simple model predictions using equation (15) and equation (22), respectively. Simulated values from SOLPS are taken from the cell in the first flux tube in the SOL at the midplane.

Substituting equations (12) and (20) into equation (19) gives:

$$n_{\mathrm{e,u}} = \frac{3}{2}\frac{f_{\mathrm{rad}}^{1/2}}{e f_{\mathrm{mom}}}\left(\frac{m_{\mathrm{D}}}{2}\right)^{1/2}\left(\frac{2\kappa_0\kappa_Z}{7L_{\mathrm{c}}}\right)^{2/7} \times \left(\frac{1.1\times10^{23}\Delta p_{\mathrm{t-d}}p_0}{\gamma b\sin\alpha_{\mathrm{t}}}\right)^{1/2} q_{||,\mathrm{u}}^{3/14}. \quad (21)$$

The model for $n_{\mathrm{e,u}}$ therefore implies that $n_{\mathrm{e,u}} \propto p_0^{1/2}$; however, $n_{\mathrm{e,u}} \propto p_0^{0.31}$ gave best agreement to measurements on AUG [52]. It was suggested that the weaker dependence on p_0 may be due to the dependence of $b \propto p_0^{1/4}$. Indeed, $b \approx 1.7p_0^{0.38}$ (corresponding to values of $b = 2-4$) provides reasonable agreement to this SOLPS-ITER database. Finally, Kallenbach assumes that the f_{rad} and f_{mom} partly cancel, which is justified since an increase in f_{rad} tends to cause a decrease in f_{mom} [46]. A value of $f_{\mathrm{rad}}^{1/2}/f_{\mathrm{mom}} \approx 0.8$ gives best agreement to the simulations. With these assumptions, $n_{\mathrm{e,u}}$ becomes:

$$n_{\mathrm{e,u}} = \left(\frac{\kappa_Z}{L_{\mathrm{c}}}\right)^{2/7} q_{||,\mathrm{u}}^{3/14}\sin\alpha_{\mathrm{t}}p_0^{0.31}\times 2\times10^{17}. \quad (22)$$

Comparison of the calculated electron density and the value at the outer midplane separatrix from SOLPS is shown in figure 8(*b*). Agreement within 25% is found across a range of densities spanning at least a factor of two. For this comparison, p_0 was calculated using equation (8), which resulted in moderately less scatter than taking the values directly from the simulation output at the pump duct location. The D_2 gas puffing location can also influence the separatrix density. Although not shown in the figure, strong puffing D_2 from the midplane did tend to increase the separatrix density up to 30 % higher than the prediction.

2.6. Detachment window

The detachment qualifier is expected to be ≈1 when the ionisation front location, L_{front}, approximated by the minimum parallel distance to the target of the 5 eV surface across the first 3 flux rings in the SOL, moves away from the target. This movement is demonstrated from the SOLPS database in figure 9, which shows strong movement away from the target as $T_{\mathrm{e,t}}$ reduces below 1 eV.

While the models in the previous subsections outline the conditions necessary for achieving detachment, they do not fully characterise the resultant divertor conditions in terms of ionisation and radiation front locations, or the robustness of the detachment state against transient changes in plasma conditions. Transient alterations in upstream power and density could arise in a reactor due to various factors, including MHD phenomena (e.g. sawteeth), fluctuations in radiation (e.g. pellet misfiring), H-L back transitions, or fluctuations in fusion power associated with discrete pellet injections, or arising from the finite resolutions of the various control systems. This section examines the amount of power that can be absorbed with a detachment front located at various points along the divertor leg. The required location of the front remains undetermined, as further understanding of the detachment control system is needed.

The Detachment Location Sensitivity (DLS) model [39, 54] is an analytical, Lengyel-type model, that can predict detachment sensitivity, defined as the degree of front movement for a given change in conditions, for a specified magnetic configuration and upstream condition. The model assumes no neutrals and a fixed-fraction impurity concentration, with radiation being the only energy loss mechanism in the system. Recently, the model has been extended (DLS-Extended, subject of a separate publication) to enable finite-width radiation regions and the capability to consider the region upstream of the X-point, thus enabling the use of argon and application to STEP. The DLS-extended solves a form of the Lengyel heat loss formula:

$$\frac{\partial\left(q_{||}/B\right)}{\partial s} = \frac{n_{\mathrm{e,u}}^2 T_{\mathrm{e,u}}^2}{T_{\mathrm{e}}^2} c_Z L_Z - W_{\mathrm{radial}} \quad (23)$$

where $L_Z(T_{\mathrm{e}})$ is the impurity cooling curve with an assumed $n_{\mathrm{e}}\tau$ value of 0.5×10^{20} m^{-3}s and W_{radial} is the radial heat source

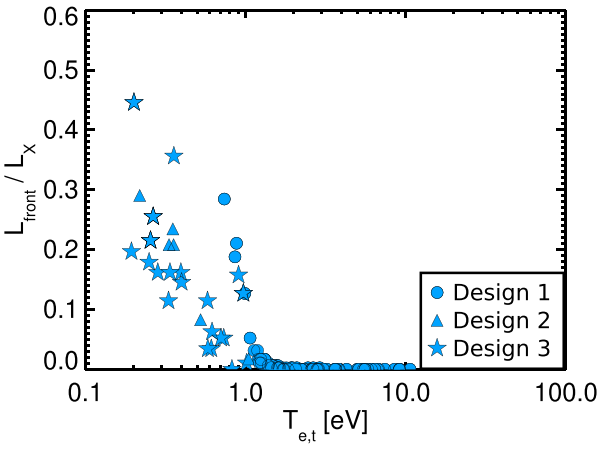

Figure 9. The parallel distance of the location of the 5 eV surface from the target, L_{front}, normalised to the parallel distance from X-point to target, is shown as a function of peak target electron temperature.

admitted to the flux tube between the midplane and the X-point:

$$W_{\text{radial}} = \frac{q_{||,\text{u}}/B_\theta}{\int_{s_x}^{L_c} \frac{1}{B} \text{d}s}. \tag{24}$$

The model defines the detachment position as the location where electron temperature reaches 0.5 eV, i.e. where virtually all of the upstream heat flux has been dissipated. Note that this defined detachment front is expected to be located behind the ionisation front (i.e. at 5 eV), and is often observed to be associated with regions of strong molecular emission.

The model was run for both the inner and outer divertor leg of the latest design. The calculation assumed an upstream density of 8×10^{19} m^{-3}, an argon concentration of 2%, and an upstream parallel energy flux density of 1.6 and 3.25 GWm^{-2} for the inner and outer divertor, respectively, based on predicted heat fluxes at the divertor entrance (i.e. near the X-point) in the first SOL ring. A detachment front position scan in $q_{||,u}$ was performed to assess the front's response to power fluctuations. The results are shown in figure 10 in terms of the required power change factor to cause reattachment and escape, defined as the front reaching the target and the X-point, respectively. While a front reaching the X-point is generally regarded as problematic due to the possibility of a radiative core collapse (with the exception of an X-point radiator [55]), in reality, a front approaching the X-point would likely cause issues earlier due to reductions in neutral compression.

Figure 10(*a*) demonstrates that an outer divertor front situated approximately halfway between the X-point and the target in poloidal space would buffer power transients increasing up to a factor of ≈1.6 and decreasing by a factor of ≈0.3 before escape. The inner divertor front is inherently less stable due to the increasing total B field as the leg moves away from the target (total flux compression). As the front moves away from the target, the lower B field enhances its radiative power and eases further movement upstream, leading to a large region of low stability indicated by both reattachment and escape lines flattening below $L_\theta < 0.6$ m in figure 10(*a*). With a sufficiently steep compression gradient, this effect becomes unstable, causing the front to continue moving through the unstable region (highlighted in red in figure 10(*a*). This instability has also previously been described and observed in SOLPS simulations [39].

In both legs, the front becomes more stable with a greater extent of detachment due to the resulting lower effective connection length [39]. As the front approaches the X-point, stabilisation occurs in the outer leg due to increasing poloidal flux expansion, while the inner leg stabilises as the radiation front extends further into the upstream region where the higher total B field reduces radiative power.

Figure 10(*c*) presents the same results as figures 10(*a*) and (*b*) but in the poloidal plane, with the front escape margin omitted for clarity. The difference in robustness between the inner and outer legs is clearly visible. While there is considerable flexibility in positioning the outer front, the inner front must be situated closer to the X-point to ensure resilience against power fluctuations. These results suggest that fully detached divertor legs in STEP should withstand regular transitions to SN on the outboard leg. However, they also indicate the necessity for further design optimisation to improve the stability and detachment window of the inner divertor target in future iterations.

3. Application of reduced models in predicting STEP exhaust scenarios

To rapidly evaluate STEP plasma exhaust conditions, both upstream and downstream, the models in section 2 have been integrated together into a single python code named `DART` (Detachment Analysis with Reduced modelling Tools [4]) which runs in ≈10 s for 100 time points. This section aims to explore conditions required for detachment in the outer divertor leg during the entire pulse. The ramp-up and ramp-down phases requires careful balancing between high-power input and low separatrix density for efficient current-drive, while maintaining divertor detachment, which favours low power and high separatrix density. During the burning flat-top phase, the exhaust conditions are evaluated with narrower SOL widths and lower core radiation fractions, and peak heat loading is investigated during a scenario simulating divertor reattachment due to a loss of Ar seeding.

The model requires several inputs that are defined as a functions of time, as outlined in table 2. The algorithm begins by assuming $c_{\text{Ar}} = 3\%$ and $p_0 = 10$ Pa, allowing for the calculation of f_{div}. Subsequently, p_0 is recalculated to ensure consistency with the input separatrix density. Following this, c_{Ar} is recalculated to achieve a solution consistent with both p_0 and the input q_{det}. The algorithm iterates the solution, with the final calculated value of c_{Ar} and p_0 serving as the initial starting values for the next iteration, until the change in c_{Ar} falls below a predefined threshold.

[4] `DART` can be accessed through: https://git.ccfe.ac.uk:shenders/dart.),

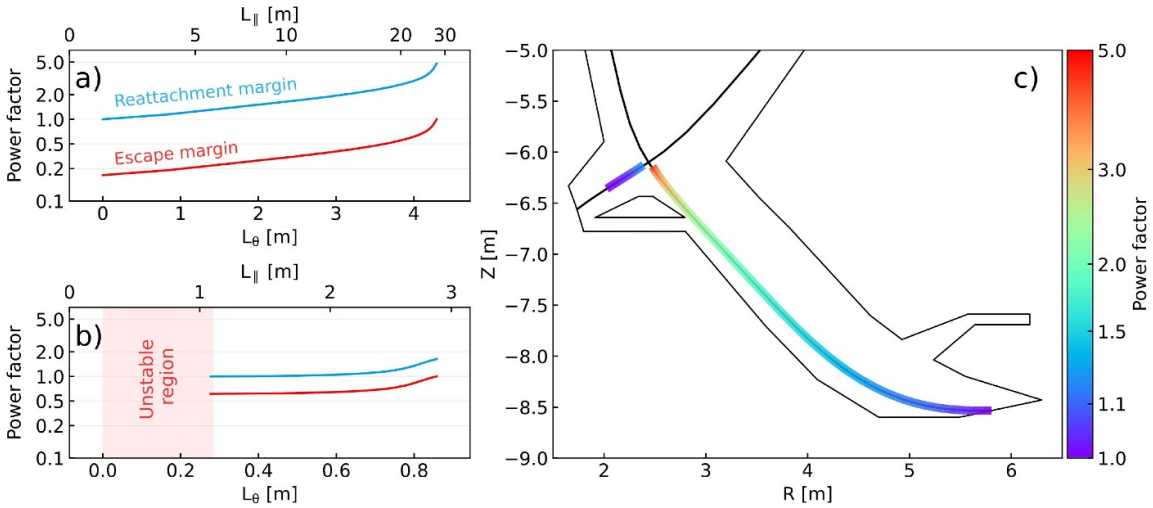

Figure 10. The power factor required to reattach the front to the target and to allow the front to escape to the X-point is shown as a function of the power change factor along both the poloidal and parallel connection lengths for the (*a*) outer divertor and (*b*) inner divertor. The same reattachment margin is illustrated in 2D poloidal R, Z space in (*c*).

Table 2. Summary of reduced exhaust model inputs and outputs.

Input	Output
I_P Plasma current	$q_{\|\|}^{\mathrm{unmit}}$ Unmitigated parallel energy flux density (equation (3))
P_sep Power crossing separatrix	f_div Power fraction to divertor (equation (5))
$n_\mathrm{e,u}$ Separatrix density	p_0 Divertor neutral pressure (equation (22))
q_det Detachment qualifier	c_Ar SOL Ar concentration (equation (7))
α_t Target grazing angle	$B_\theta \approx 0.31 I_\mathrm{P}/\kappa a_\mathrm{min}$ Poloidal magnetic field
κ Plasma elongation	$T_\mathrm{e,u}$ Upstream electron temperature (equation (15))
B_0 Toroidal magnetic field	κ_Z Finite-Z correction (equation (16) and equation (17))
R_0 Geometric radius	$q_{\perp,\mathrm{t}}$ Target heat load (equation (13))
a_min Minor radius	$T_\mathrm{e,t}$ Target temperature (equation (9))
$\lambda_\mathrm{q,u}$ SOL heat flux width	f_mom Momentum loss factor (equation (10))

An illustrative plasma scenario for the latest design with six distinct phases is presented in figure 11, where the inputs are shown in the left column and the outputs are shown in the right column. The time axis is arbitrary such that the plasma is in steady state at each time point, and the core plasma evolution is simplified such that the power crossing the separatrix, plasma current, and separatrix density change linearly during both the ramp-up and ramp-down as shown in figures 11(*a*) and (*b*). The initial and final values during the ramps are based on approximate expectations from JETTO modelling [56]. The detachment qualifier input is set to one throughout the scenario, except in phase V, which demonstrates reattachment, where it is set to five. Note that the code can only adjust the Ar concentration to find a solution that matches the input detachment qualifier. If it is not possible to achieve this, even with Ar concentration set to zero, then the code will output the divertor conditions corresponding to the pressure associated with the input separatrix density.

Phase I represents the plasma current ramp-up. Figure 11(*a*) illustrates the I_P ramp from 2–21 MA and P_sep increase from 10–70 MW, representing the required injected auxiliary heating power for current drive with an assumed core radiated power fraction of 0.5. An abrupt parameter change occurs near the top of the current ramp, signifying the transition to the burning phase II. The power crossing the separatrix is then expected to be ≈150 MW, corresponding to a fusion power of 1.7 GW, an injected power of 150 MW, and a core radiation fraction of 70 %. Figure 11(*b*) illustrates the ramp in the separatrix electron density from $1-3\times10^{19}$ m^{-3}. A further increase to 4.2×10^{19} m^{-3} then occurs during the transition to phase II.

The plasma current ramp-up results in an increase in B_p, which subsequently alters the connection length, $L_\mathrm{X} \approx 4\pi B_\mathrm{T}/B_\mathrm{p}$, and $\lambda_\mathrm{q,u}$. Values of $\lambda_\mathrm{q,u}$ were calculated using regression #9 and #14 from Eich *et al* [33], the generalised power width scaling from Eich given in equation (26), regression #2 from Thornton and Kirk [34], and predictions from the HD model [36] with $Z_\mathrm{eff} = 10$. These results are presented in figure 11(*c*). The shaded region represents the geometric mean and standard deviation of the predicted values, which is used as input to the model and defines the uncertainty in the outputs.

Three additional phases are explored during the burning phase: phase III examines a scenario where the SOL width is reduced to below 1 mm; phase IV represents conditions where the core radiation fraction is lowered from 0.7 to 0.6; and phase V involves increasing the input q_det from 1 to 5 to simulate

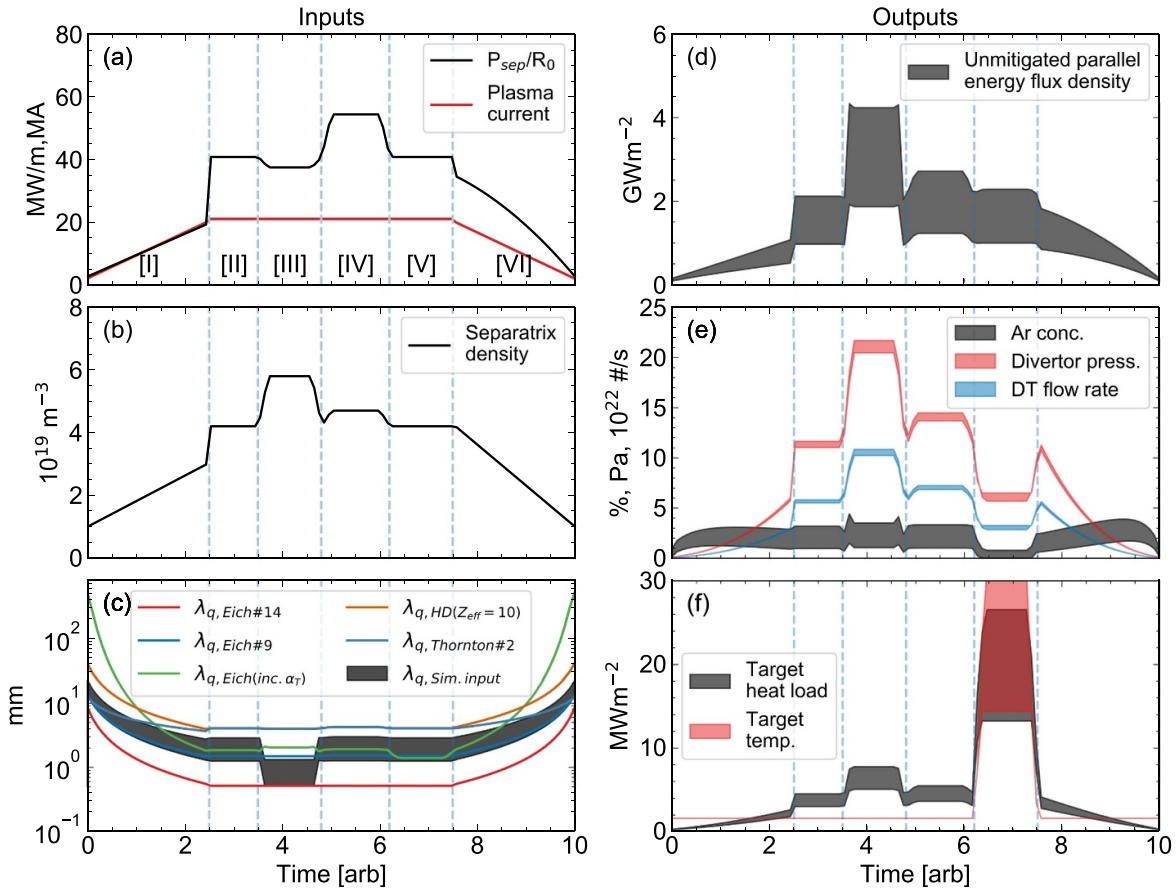

Figure 11. Simplified input time traces of a STEP plasma pulse are shown in (*a*)–(*c*), while exhaust parameters derived from reduced models are presented in (*d*)–(*f*). The time axis is presented in arbitrary units. The scenario is split into six distinct phases: [I] current ramp-up with auxiliary heating, [II] burning plasma with fusion power $P_{fus} = 1.7$ GW, auxiliary power $P_{aux} = 150$ MW, and core radiated power fraction $f_{rad,core} = 0.7$, [III] SOL width set by $\lambda_{q,Eich\#14}$ with $P_{fus} = 1.5$ GW, [IV] core radiated power fraction $f_{rad,core} = 0.6$, [V] loss of Ar seeding with fixed separatrix density, and [VI] current ramp-down with a gradual reduction in power and density. Divertor detachment is predicted throughout except for phase V, which simulates reattachment.

the extreme conditions expected during a temporary loss of Ar seeding. In the latter case, as $n_{e,u}$ remains constant, the divertor pressure decreases due to the drop in Ar concentration.

Finally, phase VI simulations the plasma current ramp-down. During the ramp-down, there is a more gradual decrease in $n_{e,u}$ compared to the ramp-up, primarily because the constraint on current-drive efficiency is lifted. Additionally, the core radiation fraction may also be reduced during the ramp-down, resulting in a more gradual decay of P_{sep} to control the H-L transition point.

The simulation outputs are shown in figures 11(*d*)–(*f*). Figure 11(*d*) illustrates the predicted unmitigated parallel energy flux density, which is lowest during the plasma current ramp-up and lies between 1 GWm^{-2} and 2 GWm^{-2} during nominal flat-top conditions. Figure 11(*e*) indicates that an Ar concentration of approximately 3% is required throughout most of the scenario. At this concentration during the current flat-top, full detachment is achievable when the neutral pressure is maintained at ≈12 Pa. Assuming a divertor-to-core enrichment factor of 3x, then $Z_{eff} \approx 4$ may be a reasonable estimate within the pedestal. For comparison, high power JET experiments demonstrated typical operation with $Z_{eff} \approx 3$ during Ar seeding experiments with c_{Ar} up to 2% in the SOL [31].

To prevent the Ar concentration from exceeding ≈3% in phases III and IV, $n_{e,u}$ is increased to raise the divertor pressure, which is limited to ≈20 Pa to avoid exceeding a puff rate of 10^{22} DT s^{-1}. As detailed in section 3.1, a pressure higher than 20 Pa could be achieved by further lowering the pump speed; however, this may impact detachment control throughout the scenario and density control during the ramp-up. Even at a divertor pressure of 20 Pa, the fusion power still needed to be reduced to the minimum value of 1.5 GW in phase III to maintain detachment. The peak heat loads associated with the detached phases ($T_{e,t} \approx 1$ eV) are shown in figure 11(*f*) and typically indicate values below 5 MWm^{-2}, with moderately higher values of ≈7.5 MWm^{-2} in phase II due to the higher separatrix density. Unsurprisingly, the highest peak heat loads, ranging from 15 MWm^{-2} to 25 MWm^{-2}, occur during phase V, which simulates reattachment. Such high peak heat loads could likely be tolerated for only 1–2 s.

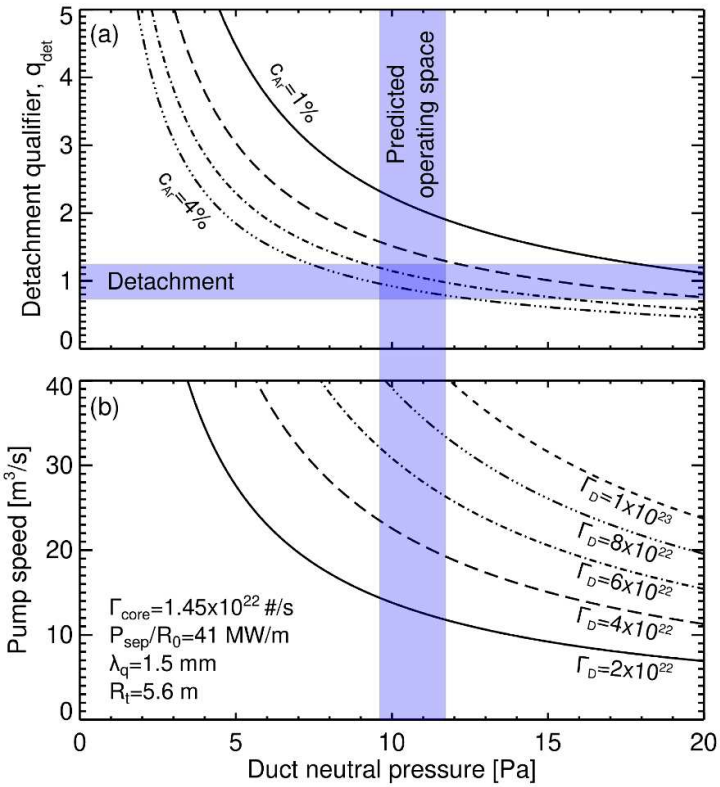

Figure 12. Calculated (*a*) detachment qualifier and (*b*) total pump speed as a function of the duct neutral pressure.

3.1. Fuel cycle requirements

Achieving ≈12 Pa at the target can be accomplished either by increasing the ratio of injected particle flux to pump speed or by altering the divertor design. The DT gas flow should be minimised to prevent excessive tritium inventory. The detachment qualifier and pump speed are shown as a function of pressure in figure 12. As indicated previously, an Ar concentration of ≈3% would be needed when operating with a divertor pressure of 12 Pa, as shown in figure 12(*a*). By rearranging equation (8) for the total pump speed, figure 12(*b*) demonstrates that the total pump speed should fall within the range of 20–25 $m^3\ s^{-1}$. In general, figure 12 illustrates the trade-offs between reducing the required Ar for detachment and minimising the total tritium inventory needed within the fuel cycle. The divertor pressure could also be increased without changing the pumping or gas flow rates by changing the divertor outer divertor target geometry relative to the pump duct location. This optimisation, along with changes to the inner divertor geometry and assessment of the necessary He pumping speed, is planned in future studies.

4. Conclusions

Results in this paper provide the first overview of the STEP divertor design and associated plasma scenario. The large set of SOLPS-ITER simulations is shown to provide a sufficient test of reduced model predictions of key exhaust parameters, such as the detachment threshold, the upstream temperature and density, and the peak heat loads. These simple reduced models can then be used to provide a fast overview of the entire plasma scenario, including the current ramp-up and ramp-down. The current STEP divertor design is shown to provide access to pronounced divertor detachment, with divertor pressures between 10 Pa and 15 Pa and Ar concentrations in the SOL of ≈3%. However, the following areas described below must be addressed in future work.

4.1. Key uncertainties

The SOL heat flux width remains a highly uncertain parameter, which will likely remain that way until experiments at higher plasma current begin to operate. Measurements of the SOL heat flux width in MAST-U plasma scenarios operating at maximum designed plasma current (≈2 MA) may reduce uncertainty. New results from high-fidelity turbulence simulations will also contribute to advancing the understanding of heat flux width predictions, as theses simulations expand to cover a broader range of scenarios.

Understanding the amount of peripheral edge temperature gradient screening of Ar expected is another key milestone. While the neoclassical predictions are well known, predictions

of the pedestal temperature and density gradients are harder to accurately predict, especially in plasma regimes with significant impurity content.

Initial simulations with particle drifts for STEP represent a major step forward in understanding, however these simulations have currently studied cases with D-only; a fixed fraction of Ar is applied to facilitate simulations with detached divertors. Future work assessing the impact of drifts on simulations with fully evolving impurities remains a top priority. Furthermore, understanding how drifts change the solution in SN is another goal to better understand the risk of the plasma transiently moving between double-null and SN during the scenario.

Uncertainties in other key simulation assumptions also remain. It is evident that significant errors are present in the molecular rate coefficients used by 2D exhaust codes [57], and their impact on the overall solution is not yet well characterised. Primarily, a change in these molecular rates could result in deeper detachment than predicted, and to a lesser extent could alter the detachment threshold. The atomic rate coefficients for medium weight species, such as Ar, could also have significant uncertainty. The impact of assuming different temperatures for different impurity charge states is currently unknown. Finally, plasma kinetic effects are not properly captured in SOLPS-ITER, which could impact the impurity confinement within the divertor.

4.2. Future design optimisation

The inclusion of a dome in the STEP divertor is a recent advancement, and its shape, neutral transmission, and the inner strike-point position have yet to be optimised. The dome will ultimately involve a trade-off between pumping efficiency and detachment access [58]; currently, the inner divertor detaches early and is a significant source of helium in the core. The trade-off between detachment access and pumping efficiency is also impacted by the position of the pump duct location. Future simulations of STEP should focus on optimising this trade-off, with particular emphasis on He pumping.

Acknowledgments

The lead author would like to acknowledge many insightful discussions with Dr Geoff Fishpool. This work has been funded by STEP, a major technology and infrastructure programme led by UK Industrial Fusion Solutions Ltd (UKIFS), which aims to deliver the UK's prototype fusion powerplant and a path to the commercial viability of fusion.

Appendix.Near SOL power width

3D gyrokinetic and fluid turbulence simulations for ITER and other large devices predict significantly higher values of $\lambda_{q,u}$ compared to experimental scalings [59, 60]. The hypothesis suggests that while current scalings are dominated by drift-driven transport, large devices may instead experience turbulence-driven transport. The critical heat flux diffusion, at which anomalous transport exceeds neoclassical drifts, can be approximated as:

$$\chi_{crit} \approx \nu_D \lambda_{q,u} = T_{e,sep}\lambda_{q,u}/RB. \tag{25}$$

Here, ν_D is the drift velocity estimated from the magnetic drift, consistent with equation 2 from Xu *et al* [60]. Using the two-point model to estimate the separatrix temperature, $T_{e,sep}$ (see equation (15)), a temperature of ≈250 eV is expected for STEP with $\lambda_{q,u} = 2$ mm, resulting in a critical heat flux diffusion of $\approx 0.04\ m^2\ s^{-1}$. This value is comparable to those found for JET and C-Mod using the same method but significantly higher than those predicted for ITER and EU DEMO. A smaller $\lambda_{q,u} = 0.5$ mm results in $T_{sep} \approx 350$ eV and a critical heat flux value of $\approx 0.015\ m^2\ s^{-1}$, which aligns with predictions for ITER and DEMO, where turbulence is expected to broaden the SOL.

The effect of turbulence on SOL broadening has also been studied experimentally by Eich *et al* [35], who proposed a generalised power width scaling:

$$\lambda_{q,u} = \frac{2}{7}\rho_{s,pol}\left(1 + (2.1 \pm 0.15)\,\alpha_T^{1.7\pm0.19}\right) \times (2.1 \pm 0.09), \tag{26}$$

where $\rho_{s,pol} = \sqrt{m_D T_{e,sep}}/eB_{\theta,u} \approx 1.75$ mm using $T_{e,sep} = 250$ eV. The turbulence parameter α_T is approximated using:

$$\alpha_T \approx 3 \times 10^{-18} q_{cyl}^2 R n_{e,sep} Z_{eff}/T_{e,sep}^2. \tag{27}$$

$q_{cyl} = B_0\kappa/B_{theta,u}a_{min} \approx 4$ is the cylindrical safety factor. Using a separatrix electron density of $n_{sep} = 3 \times 10^{19}\ m^{-3}$ and assuming a high $Z_{eff} = 5 - 10$ consistent with high Ar seeding, $\alpha_T \approx 0.4 - 0.8$. With these values, the scaling predicts $\lambda_{q,u}$ in the range of $1.4 - 2.4$ mm.

It is also important to note that if the SOL becomes ideal MHD unstable, transport is likely to increase, broadening the SOL width. The MHD stability limit can be estimated using the ideal ballooning parameter [61, 62]:

$$\alpha_{MHD} = \frac{q_{cyl}^2 R}{\lambda_{p,u}} \frac{4\mu_0 p_{e,u}}{B_{tot,u}^2}, \tag{28}$$

where an ideal MHD instability occurs above a critical value of α. $p_{e,u}$ is the separatrix pressure and $\lambda_p \approx 2\lambda_{q,HD}$ is the pressure decay length [63]. The critical value is calculated using a fit to global numerical calculations: [63, 64]:

$$\alpha_{crit} = \kappa^{1.2}\,(1 + 1.5\delta)\,. \tag{29}$$

STEP is predicted to operate with $\alpha_{crit} \approx 6.8$, assuming a triangularity of $\delta = 0.5$. With $n_{sep} = 3 \times 10^{19}\ m^{-3}$, $\alpha_{MHD} = \alpha_{crit}$ when $\lambda_{q,u} = 1.2$ mm, indicating that short heat flux decay lengths may be unstable.

ORCID iDs

S.S. Henderson https://orcid.org/0000-0002-8886-1256
L. Xiang https://orcid.org/0000-0001-8175-6640

C. Ridgers https://orcid.org/0000-0002-4078-0887
J. Karhunen https://orcid.org/0000-0002-4525-8158
H. Meyer https://orcid.org/0000-0002-5565-1199
D. Vaccaro https://orcid.org/0009-0007-2171-794X
F. Perez Smith https://orcid.org/0009-0001-2218-7203
J. Harrison https://orcid.org/0000-0003-2906-5097
B. Lipschultz https://orcid.org/0000-0001-5968-3684

References

[1] Pitts R.A. *et al* 2019 *Nucl. Mater. Energy* **20** 100696
[2] Asakura N., Hoshino K., Kakudate S., Subba F., You J.-H., Wiesen S., Rognlien T.D., Ding R. and Kwon S. 2023 *Nucl. Mater. Energy* **35** 101446
[3] Wenninger R. *et al* 2014 *Nucl. Fusion* **54** 114003
[4] Wenninger R. *et al* 2017 *Nucl. Fusion* **57** 046002
[5] Loarte A. *et al* 2007 *Nucl. Fusion* **47** S203
[6] Siccinio M. *et al* 2020 *Fusion Eng. Design* **156** 111603
[7] Reimerdes H. *et al* 2020 Nucl. Fusion **60** 066030
[8] Militello F. *et al* 2021 *Nucl. Mater. Energy* **26** 100908
[9] Xiang L. *et al* 2021 *Nucl. Fusion* **61** 076007
[10] Mantilla L.A *et al* 2021 *Nucl. Mater. Energy* **26** 100886
[11] Meyer H. 2023 The plasma scenarios for the spherical tokamak for energy production (STEP) and their technical implications *IAEA Fusion Energy Conf. London* EX-C (available at: https://conferences.iaea.org/event/316/contributions/28532/attachments/14896/24185/Meyer-H-EX-C.pdf)
[12] Meyer H. 2024 *Phil. Trans. R. Soc.* A **382** 20230406
[13] Siccinio M., Graves J.P., Kembleton R., Lux H., Maviglia F., Morris A.W., Morris J. and Zohm H. 2022 *Fusion Eng. Des.* **176** 113047
[14] Lennholm M. *et al* 2024 *Nucl. Fusion* **64** 096036
[15] Hudoba A. *et al* 2023 *Nucl. Mater. Energy* **35** 101410
[16] Hudoba A. *et al* 2024 *Nucl. Fusion* **64** 086055
[17] Siccinio M., Fable E., Lackner K., Scarabosio A., Wenninger R.P. and Zohm H. 2016 *Plasma Phys. Control. Fusion* **58** 125011
[18] Wiesen S. *et al* 2015 *J. Nucl. Mater* **463** 480
[19] Bonnin X., Dekeyser W., Pitts R., Coster D., Voskoboynikov S. and Wiesen S. 2016 *Plasma Fusion Res* **11** 1403102
[20] Kirschner A. *et al* 2023 *Nucl. Fusion* **63** 126055
[21] Glugla M. *et al* 2006 *Fusion Eng. Des.* **81** 733
[22] Pacher H.D. *et al* 2015 *J. Nucl. Mater.* **463** 591
[23] Day C. and Giegerich T. 2014 *IEEE Trans. Plasma Sci.* **42** 1058
[24] Kallenbach A. *et al* 2024 *Nucl. Fusion* **64** 056003
[25] Dux R., Loarte A., Angioni C., Coster D., Fable E. and Kallenbach A. 2017 *Nucl. Mater. Energy* **12** 28
[26] Field A.R. *et al* 2023 *Nucl. Fusion* **63** 016028
[27] Osawa R.T., Moulton D., Newton S.L., Henderson S.S., Lipschultz B. and Hudoba A. 2023 *Nucl. Fusion* **63** 076032
[28] Karhunen J. *et al* 2024 Nucl. Fusion **64** 096021
[29] Kallenbach A. *et al* 2015 *Nucl. Fusion* **55** 053026
[30] Henderson S.S. *et al* 2023 *Nucl. Fusion* **63** 086024
[31] Henderson S.S. *et al* 2024 *Nucl. Fusion* **64** 066006
[32] Stangeby P.C. 2000 *Taylor and Francis*
[33] Eich T. *et al* 2013 *Nucl. Fusion* **53** 093031
[34] Thornton A.J. and Kirk A. 2014 *Plasma Phys. Control. Fusion* **56** 055008
[35] Eich T., Manz P., Goldston R.J., Hennequin P., David P., Faitsch M., Kurzan B., Sieglin B. and Wolfrum E. 2020 *Nucl. Fusion* **60** 056016
[36] Goldston R.J. 2012 *Nucl. Fusion* **52** 013009
[37] Kallenbach A. *et al* 2016 *Plasma Phys. Control. Fusion* **58** 045013
[38] Scarabosio A. *et al* 2009 *J. Nucl. Mater.* **390** 494
[39] Cowley C., Lipschultz B., Moulton D. and Dudson B. 2022 *Nucl. Fusion* **62** 086046
[40] Reimerdes H. *et al* 2017 *Nucl. Fusion* **57** 126007
[41] Kallenbach A. *et al* 2013 *Plasma Phys. Control. Fusion* **55** 124041
[42] Temmerman G.D., Kirk A., Nardon E. and Tamain P. 2011 *J. Nucl. Mater.* **415** S383
[43] Henderson S *et al* 2024 *Nucl. Mater. Energy* **41** 101765
[44] Henderson S.S. *et al* 2021 *Nucl. Mater. Energy* **28** 101000
[45] Stangeby P.C. 1993 *Nucl. Fusion* **33** 1695
[46] Lipschultz B. *et al* 2007 *Fusion Sci. Technol.* **51** 369
[47] Osawa R.T., Newton S.L., Moulton D., Henderson S.S., Badicel V. and Hudoba A. 2024 *Nucl. Fusion* **64** 106007
[48] Newton S. *et al* 2024 private communication
[49] Eich T., Sieglin B., Thornton A.J., Faitsch M., Kirk A., Herrmann A. and Suttrop W. 2017 *Nucl. Mater. Energy* **12** 84
[50] Loarte A. *et al* 2014 Nucl. Fusion **54** 033007
[51] Komm M. *et al* 2023 *Nucl. Fusion* **63** 126018
[52] Kallenbach A. *et al* 2018 *Plasma Phys. Control. Fusion* **60** 045006
[53] Kallenbach A. *et al* 2019 *Nucl. Mater. Energy* **18** 166
[54] Lipschultz B., Parra F.I. and Hutchinson I.H. 2016 *Nucl. Fusion* **56** 056007
[55] Bernert M. *et al* 2020 *Nucl. Fusion* **61** 024001
[56] Tholerus E. *et al* 2024 *Nucl. Fusion* **64** 106030
[57] Verhaegh K. *et al* 2024 *Nucl. Fusion* **64** 086050
[58] Kukushkin A.S. and Pacher H.D. 2016 *Nucl. Fusion* **56** 126012
[59] Chang C. *et al* 2017 *Nucl. Fusion* **57** 116023
[60] Xu X., Li N.M., Li Z.Y., Chen B., Xia T.Y., Tang T.F., Zhu B. and Chan V.S. 2019 *Nucl. Fusion* **59** 126039
[61] Rogers B.N., Drake J.F. and Zeiler A. 1998 *Phys. Rev. Lett.* **81** 4396
[62] LaBombard B., Hughes J.W., Mossessian D., Greenwald M., Lipschultz B. (J.L. Terry and the Alcator C-Mod Team) 2005 *Nucl. Fusion* **45** 1658
[63] Eich T., Goldston R.J., Kallenbach A., Sieglin B. and Sun H.J. 2018 *Nucl. Fusion* **58** 034001
[64] Bernard L.C., Helton F.J., Moore R. and Todd T. 1983 *Nucl. Fusion* **23** 1475